



**HAL**  
open science

## Stress fibres are embedded in a contractile cortical network

Timothée Vignaud, Calina Copos, Christophe Leterrier, Mauricio Toro-Nahuelpan, Qingzong Tseng, Julia Mahamid, Laurent Blanchoin, Alex Mogilner, Manuel Théry, Laetitia Kurzawa

► **To cite this version:**

Timothée Vignaud, Calina Copos, Christophe Leterrier, Mauricio Toro-Nahuelpan, Qingzong Tseng, et al.. Stress fibres are embedded in a contractile cortical network. *Nature Materials*, 2021, 20, pp.410-420. 10.1038/s41563-020-00825-z . hal-02975993

**HAL Id: hal-02975993**

**<https://hal.science/hal-02975993>**

Submitted on 13 Nov 2020

**HAL** is a multi-disciplinary open access archive for the deposit and dissemination of scientific research documents, whether they are published or not. The documents may come from teaching and research institutions in France or abroad, or from public or private research centers.

L'archive ouverte pluridisciplinaire **HAL**, est destinée au dépôt et à la diffusion de documents scientifiques de niveau recherche, publiés ou non, émanant des établissements d'enseignement et de recherche français ou étrangers, des laboratoires publics ou privés.



Distributed under a Creative Commons Attribution 4.0 International License

# 1           **Stress fibers are embedded in a contractile cortical network.**

2  
3   Timothée Vignaud<sup>1,2,3</sup>, Calina Copos<sup>4</sup>, Christophe Leterrier<sup>5</sup>, Mauricio Toro-Nahuelpan<sup>6</sup>,  
4   Qingzong Tseng<sup>1,2</sup>, Julia Mahamid<sup>6</sup>, Laurent Blanchoin<sup>1,2</sup>, Alex Mogilner<sup>4\*</sup>, Manuel  
5   Théry<sup>1,2\*</sup> and Laetitia Kurzawa<sup>1,2\*</sup>

6  
7   <sup>1</sup> CytoMorpho Lab, Laboratoire de Physiologie cellulaire et Végétale, Interdisciplinary Research Institute of  
8   Grenoble, CEA, CNRS, INRA, Grenoble-Alpes University, Grenoble, France.

9   <sup>2</sup> CytoMorpho Lab, Human Immunology Physiopathology and Immunotherapy, Institut de Recherche Saint  
10   Louis, University of Paris, CEA, INSERM, F-75475, Paris, France.

11   <sup>3</sup> Clinique de chirurgie digestive et endocrinienne, Hôtel Dieu, Nantes, 44093, France.

12   <sup>4</sup> Courant Institute and Department of Biology, New York University, New York, NY, United States of America.

13   <sup>5</sup> Aix Marseille Université, CNRS, INP UMR7051, NeuroCyto, Marseille, France

14   <sup>6</sup> Structural and Computational Biology Unit, European Molecular Biology Laboratory (EMBL), 69117  
15   Heidelberg, Germany.

16  
17   \* correspondence should be addressed to: mogilner@cims.nyu.ed, manuel.thery@cea.fr, laetitia.kurzawa@cea.fr

18  
19  
20           Contractile actomyosin networks are responsible for the production of intracellular  
21   forces. There is increasing evidence that bundles of actin filaments form interconnected and  
22   interconvertible structures with the rest of the network. In this study, we explored the  
23   mechanical impact of these interconnections on the production and distribution of traction  
24   forces throughout the cell. By using a combination of hydrogel micropatterning, traction-force  
25   microscopy and laser photoablation, we measured the relaxation of traction forces in response  
26   to local photoablations. Our experimental results and modeling of the mechanical response of  
27   the network revealed that bundles were fully embedded along their entire length in a  
28   continuous and contractile network of cortical filaments. Moreover, the propagation of the  
29   contraction of these bundles throughout the entire cell was dependent on this embedding. In  
30   addition, these bundles appeared to originate from the alignment and coalescence of thin and  
31   unattached cortical actin filaments from the surrounding mesh.

32

33

34 Contractile forces are produced mainly by actomyosin bundles or stress fibers in  
35 adherent cells <sup>1-3</sup>, and by a cortical meshwork of randomly oriented filaments in poorly-  
36 adherent cells <sup>4,5</sup>. The mechanism regulating the production and transmission of local forces  
37 throughout the cell is still poorly understood <sup>6-8</sup>. The progress in understanding this  
38 integration process has notably been limited by the technical challenges to manipulate the  
39 network locally while simultaneously measuring the impact on force production at the level of  
40 the entire cell.

41 Stress fibers are formed by the interaction and merging of pre-existing radial fibers  
42 and transverse arcs <sup>9-12</sup>. Transverse arcs are formed by the alignment and compaction of  
43 filaments at the cell front, as they are pulled by the actin network retrograde flow against cell  
44 anchorages <sup>13,14</sup>. As a result, actomyosin networks are composed of interconnected contractile  
45 elements that span the entire cytoplasm and serve as a template to transmit mechanical forces  
46 over long cellular distances <sup>15-17</sup>. Laser photoablation experiments have indeed demonstrated  
47 that the photoablation of a single stress fiber could compromise the entire traction force field  
48 <sup>18,19</sup> and lead to variations in tension in all focal adhesions including those that are not at the  
49 ends of the ablated fibers <sup>20</sup>. Similarly, stretching cells unidirectionally can lead to tension  
50 increase in all focal adhesions whatever their orientation <sup>21</sup>. Hence, directional forces along  
51 specific actomyosin bundles can propagate to other bundles with which they are inter-  
52 connected. As a consequence, the tension in a stress fiber does not only depend on forces  
53 produced in that fiber but also on the connection and orientation of adjacent fibers <sup>22</sup>. This  
54 high degree of connection between actomyosin bundles can provide the mechanical coherence  
55 at the level of the cell <sup>23-25</sup>. However, it is yet unclear how forces are transmitted from one  
56 stress fiber to the other.

57 Theoretical models of contractile networks have proposed two main paradigms to  
58 capture the mechanisms of force production and transmission in cells. In one paradigm,  
59 discrete models, that include high level details on the structure of the network, offer an  
60 accurate description of the stress fiber as a load-bearing structure and of the traction forces  
61 exerted on its anchorages to the extra-cellular matrix <sup>26-30</sup>. These models are successful at  
62 providing a description in fine details of local force production, but fail to provide a global  
63 description of the traction-force field. In the other paradigm, continuous models provide a  
64 more global view of the contractile networks by incorporating only a few coarse-grained  
65 biophysical parameters. These models work well for describing force variations with changes  
66 in cell size and shape <sup>31-33</sup>, but require focal adhesions to be taken into account to be more  
67 accurate <sup>34</sup>. These considerations suggest that the limitations of the discrete and the  
68 continuous models could be overcome by developing an intermediate model which takes into  
69 account both features of the network.

70

## 71 **Results**

### 72 **Cells with stress fibers produce high contractile forces**

73 We first tested experimentally if the presence of actin bundles could impact the  
74 magnitude and distribution of traction forces as compared to a more homogeneous network of  
75 the same size and shape<sup>32,33</sup>. To that end, cells were plated on either dumbbell-shaped or pill-  
76 shaped micropatterns fabricated on poly-acrylamide hydrogel. The size of the micropatterns,  
77 60 $\mu$ m-long, corresponded to the average length of cells on poly-acrylamide gel  
78 homogeneously coated with fibronectin (Extended Data 1a-c). The dumbbell-shaped  
79 micropattern was designed to promote in the cell the assembly of two stress fibers, which are  
80 known to form preferentially above non-adhesive zone<sup>35,36</sup>, whereas the pill-shaped  
81 micropattern was designed to promote a more homogeneous network of actin filaments  
82 (Figure 1a). Both micropatterns were devised to promote the cells adopting the same shape.

83 As expected, two main peripheral stress fibers and only a few smaller and thinner  
84 internal bundles were formed in cells plated on dumbbell-shaped micropatterns. These  
85 structures were localised in the ventral side of the cells and concentrated crosslinkers of actin  
86 filaments and myosins<sup>37</sup>. By contrast, numerous, more evenly distributed but thinner bundles  
87 of actin filaments were formed in cells on pill-shaped micropatterns (Figure 1b and Extended  
88 Data 1). The contractility generated by these cells forming two distinct cytoskeletal networks  
89 enclosed in a similar envelope was measured using traction force microscopy. As illustrated  
90 by the averaged traction-force maps and quantified by the mechanical energy that was  
91 transferred to the hydrogel, significantly higher mechanical energy was generated by cells  
92 containing the stress fibers (dumbbell micropattern) than the cells without (pill micropattern;  
93 Figure 1c, d). Similar changes were observed with other micropattern geometries in which the  
94 modulation of the size and position of non-adhesive zones affected the production of stress  
95 fibers (Extended Data 1d). This result indicated that the organization of actomyosin  
96 components into stress fibers, in response to local variations of substrate adhesiveness, plays a  
97 major role in setting the magnitude of force a cell could generate and transmit to the substrate.  
98 However, these global force measurements could not reveal the quantitative contribution of  
99 individual stress fibers to the total force produced by the cells.

### 100 **Stress fibers are connected to surrounding actin network**

101 By combining photoablation of the peripheral stress fibers with traction-force  
102 measurements, we assessed the specific contribution of these fibers to the global mechanical  
103 energy produced by cells plated on dumbbell micropatterns. A stress fiber was severed mid-  
104 length by localized pulsed-laser photoablation at 355 nm (see Video 1), and the release in  
105 fiber tension was captured by the relaxation in the hydrogel substrate (Figure 1e and Video 2).  
106 Surprisingly, the released energy from the cut of one of the two peripheral stress fibers was  
107 about 25 % of the total mechanical energy generated by the cell (Figure 1e, f), and was  
108 substantially lower than the expected 50% assuming the two peripheral stress fibers generate  
109 most of the mechanical energy.

110 This prompted us to investigate in more detail the relaxation of the severed stress  
111 fiber. Marks were photobleached along the fiber to monitor the entire relaxation pattern after  
112 the severing,<sup>38</sup> (Figure 2a). As previously described, the retraction of a severed end was  
113 characteristic of a visco-elastic relaxation<sup>19,39,40</sup> (Figure 2b). Indeed, the parts of the fiber  
114 distal to the photoablation displayed minimal if any relaxation (Figure 2b, 2c), and contrasted  
115 with what would have been expected with a stress fiber in isolation, in that the relaxation  
116 should be independent of the distance from the photoablation (Figure 2c). Hence, this result  
117 suggested that the fiber was not isolated but connected along its length to force-bearing  
118 elements which resisted the deformation when the fiber was severed. Similar observations  
119 have been made elsewhere in cells spread on uniform extra-cellular matrix coating<sup>38</sup>. In this  
120 work, stress fibers appeared to be connected to the extra-cellular matrix via focal adhesion-  
121 like complexes which acted as elastic linkers, and were shown to accumulate zyxin at their  
122 severed ends following photoablation at locations where new adhesions were formed.  
123 However, with the dumbbell micropattern, stress fibers were above a non-adhesive substrate,  
124 precluding the possibility of transmembrane adhesions forming at the severed ends. This led  
125 us to hypothesize that peripheral stress fibers were not connected to the extra-cellular  
126 environment but to cortical actin filaments.

### 127 **Cut stress fibers are still under tension**

128 Importantly, and in contrast to the classical view of stress fibers pulling on focal  
129 adhesions only, the stress-fiber connection to adjacent actin cytoskeletal elements implied that  
130 photoablation should redistribute the tension of the fiber to the surrounding meshwork. As a  
131 result, the remaining parts of the severed fiber should still be under tension. To test this  
132 prediction, two photoablations were performed sequentially less than a minute apart on the  
133 same fiber. In confirmation of the prediction, a noticeable release of energy was associated  
134 with the second photoablation (Figure 2d). However, the amount of energy that was released  
135 by the second photoablation was much lower than the first one because the severed fiber had  
136 already relaxed and lost some of its elastic energy. To investigate whether this lower amount  
137 of energy release resulted from a non-specific injury to the cell due to the photoablations, the  
138 second photoablation was performed on the other intact fiber. In that case, approximately the  
139 same amount of energy was released as that after the first photoablation showing that the first  
140 photoablation did not impact cell integrity (Figure 2e).

141 Previous work has suggested that discrete connections of a peripheral stress fiber to  
142 other internal fibers can affect its relaxation pattern after severing<sup>22,41</sup>. However, the  
143 incomplete relaxation pattern of the severed peripheral stress fibers we observed here was not  
144 systematically associated with interconnections with internal fibers, as illustrated by the  
145 absence of visible fibers connected to the peripheral stress fibers in Figure 2a. This led us to  
146 hypothesize that a stress fiber was connected to a low-density and widespread actin  
147 meshwork. This hypothesis was addressed by disconnecting the stress fiber from the  
148 meshwork through photoablation of a narrow region medial and parallel to the length of the  
149 fiber above the non-adhesive substrate on the hydrogel (a process we termed fiber shaving;  
150 Figure 2f and Video 3). With two successive photoablations of the stress fiber, the release of

151 energy after the second photoablation was significantly lower when the fiber had been shaved  
152 first (Figure 2g, h), supporting the hypothesis that low-density fibers connections to the  
153 peripheral stress fiber prevented its complete relaxation after it was severed.

#### 154 **Modeling the stress fibers embedding in an elastic meshwork**

155 To investigate the properties of such a network of actin fibers embedded in a cortical  
156 meshwork, we built on the ideas developed in <sup>28,38</sup> to create a new biophysical model. In this  
157 model, and in contrast with previous ones, the stress fibers were not connected to the extra-  
158 cellular matrix but to the adjacent cortical meshwork. The cortical meshwork was described  
159 as a two-dimensional (2D) ensemble of elastic links connected by nodes. The stress fibers  
160 were modeled as elastic cables under tension and connected in series. The stress fibers were  
161 connected uniformly along their length to the cortical meshwork by elastic links (Figure 3a;  
162 described in detail in Supplementary Methods).

163 We first tested the response of our model to fiber severing by locally reducing the  
164 stiffness by 90% in one of the stress-fiber elements (Figure 3b). As in the experimental set up,  
165 mechanical energy was released but was significantly less than 50%, even though in the  
166 model, it was exclusively produced by the two peripheral fibers (Figure 3b). The model also  
167 accurately accounted for the limited retraction of the fiber at distal points from the site of the  
168 simulated photoablation (Figure 3c). Furthermore, the model captured the additional release  
169 of energy after a second photoablation of the same fiber (Figure 3d).

170 Other experimental observations prompted further investigations of the model. In the  
171 experimental set up, the release in tension was not equivalent on the two severed parts of the  
172 stress fiber, and was not restricted to its distal ends: rather, the release in tension appeared  
173 higher at the end that was closer to the photoablation and extended to the other side of the cell  
174 (Figure 3e and other examples in Extended Data 2). By contrast, an isolated stress fiber would  
175 be expected to release the same amount of tension at both ends. This suggested that the  
176 cortical meshwork had an impact not only on the magnitude but also on the spatial  
177 distribution of traction-force production. To quantify this spatial effect in the model, the cell  
178 area was partitioned into four quadrants and the relative traction-force loss was measured in  
179 each quadrant as a percent amount of total traction-force loss in the cell (Figure 3f, g).  
180 Intriguingly, the model could barely account for the asymmetric traction-force loss at the end  
181 of the severed stress fiber (Figure 3f) and no traction-force loss occurred on the other side of  
182 the cell where the stress fiber was intact (Figure 3g). In addition, although we could define a  
183 given set of parameters for network elasticity that could account qualitatively for the various  
184 trends of traction-force relaxation, the traction-force changes were only in limited quantitative  
185 agreement with the equivalent experimental measurements (Figure 3b, d, f, g). Puzzled by the  
186 discrepancy between the predictions of the model and the measured loss of traction force on  
187 the other half of the cell after fiber photoablation, we decided to further interrogate the  
188 mechanical nature of the cortical meshwork.

## 189 **The cortical meshwork is contractile**

190 A local ablation in the cortical meshwork did not release a significant amount of  
191 energy as compared to the same ablation in a peripheral stress fiber (Extended Data 3a).  
192 However, the shaving of a stress fiber, i.e. the longitudinal photoablation of the cortical  
193 meshwork, led to a significant release of contractile energy (Figure 4a and b). This release  
194 was comparable to that of fiber ablation. This result showed that the cortical meshwork was  
195 contractile and not passively elastic as initially hypothesized. It also meant that the cortical  
196 meshwork actively participated in the production of traction forces. Indeed, the release of  
197 mechanical energy after a single ablation and shaving of the stress fiber were additive (Figure  
198 4a, b and Video 4), and consistent with the theoretical expectation these photoablations  
199 disrupted half of the contractile network (Figure 4a). The contractility of the cortex could also  
200 be revealed by impairing its branched architecture. The chemical inhibition of Arp2/3  
201 complex increased the global cell contractile energy although it did not affect the amount of  
202 energy released by peripheral fiber ablation, suggesting that the global increase was  
203 specifically due to the reorganisation of the cortex (Extended Data 3b). Furthermore, moving  
204 the position of the bar of the dumbbell shape did not affect the peripheral fibers, but changed  
205 the area of the cortex they were connected to. As a result, the fiber associated with a larger  
206 part of the cortex released more energy when ablated, further showing that the cortex  
207 contributed to the production of force along the fiber (Extended Data 3c).

208 Hence, we revised our initial *elastic* model by including contractility as a function of  
209 the cortical mesh (Figure 4c). The links in the cortical mesh were thus considered as  
210 contractile cables; i.e. tensed elastic springs in series with contractile elements (Figure 4c). In  
211 this second *contractile* model, the spring constants and contractilities of the cortical mesh and  
212 fiber-mesh links were the same, and different from those characterizing the stress fibers. The  
213 estimations of the magnitude and localization of mechanical-energy release based on this  
214 contractile model were in better agreement with the experimental data; including that the  
215 contractile energy released after stress fiber ablation was lower than in the elastic model,  
216 (Figure 4d), and the contractile energy released after stress fiber shaving was higher than in  
217 the elastic model (Figure 4e). As with the elastic model, the contractile model accounted  
218 correctly for the difference in contractile-energy release after the second photoablation  
219 whether it was applied to the same or opposite stress fiber. However, the amount of  
220 contractile-energy released in these scenarios was in better agreement with experimental data  
221 with the contractile model than with the elastic model (Figure 4f and g). More importantly,  
222 the contractile model captured key features of the spatial distribution of traction-force loss in  
223 response to a single photoablation in contrast to the elastic model. The contractile model  
224 recapitulated the asymmetry of traction-force loss at both ends of the severed fibers (Figure  
225 4h) and the significant traction-force loss registered on the opposite side of the cell (Figure  
226 4i). In addition, with the scenario of shaving the stress fiber prior to an off-center  
227 photoablation of that fiber (Extended Data 4a), the contractile model, in comparison with the  
228 elastic model, better accounted for the left-right symmetrical loss of traction force (Extended  
229 Data 4b; see also Figure 3f), and captured the loss of traction force at the opposite side of the  
230 cell (Extended Data 4c).

231 The theoretical modelling combined with the experimental observations supported the  
232 hypothesis that the stress fibers and the cortical meshwork were mechanically similar in that  
233 they were both elastic and contractile. Therefore the stress fibers and the cortical meshwork  
234 may not be distinct networks with discrete interconnections, but part of a single integrated  
235 network, in which architecture and mechanics of actomyosin arrays vary in space.

### 236 **The cortical meshwork forms a continuum with stress fibers**

237 To investigate further the physical interplay between stress fibers and the cortical  
238 meshwork, fixed cells were imaged at the resolution of single actin filaments by cryo-electron  
239 tomography of micropatterned cells<sup>42</sup>. It revealed that stress fibers were connected via  
240 multiple filaments to the meshwork that covers the plasma membrane (blue arrows in Figure  
241 5a). Stress fibers did not appear as isolated structure but instead formed a continuous structure  
242 with the cytoplasmic meshwork (Figure 5b, Extended Data 5 and Video 5). The density of  
243 filaments decreased progressively from the inner part of the fiber to the cytoplasmic  
244 meshwork (blue arrows in Figure 5b). Fine intracellular architecture were also analyzed by  
245 stochastic optical reconstruction microscopy (STORM). Instead of two distinct networks on  
246 top of each others, the imaging revealed that stress fibers were fully entangled in the cortical  
247 meshwork. In the cortex, filaments formed bundles which were progressively more  
248 longitudinally-aligned with closer proximity to the peripheral stress fiber (Figure 5c). Similar  
249 continuous architectures, with progressive alignment of cortical filaments in the cortex up to  
250 their interlacing with the bundles forming the stress fibers were also observed with STORM  
251 in other cell types and in the absence of adhesive micro-pattern (Figure 5d).

252 We then studied the similarities and differences in the structure and composition of the  
253 cortical meshwork and the stress fibers. RPE1 cells on dumbbell-shaped micropattern were  
254 immunostained for phospho-myosin light chain and alpha-actinin. With high-resolution  
255 confocal microscopy, although the density of actin filaments was lower in the region between  
256 the two stress fibers and appeared darker compared to the high intensity of the two fibers, a  
257 meshwork of bundles and filaments could be visualized at higher signal saturation, together  
258 with numerous patches of alpha-actinins and myosin (Figure 5e, top). Consistent with this  
259 observation, the down-regulation of the expression of alpha-actinins increased the contraction  
260 of both the cortex and the stress fibers (Extended Data 3d). These observations confirmed that  
261 although their architectures were different, the stress fibers and the central mesh shared  
262 several key molecular players involved in the regulation of their contraction.

263 Live imaging further supported our conclusion of the stress fibers being embedded in  
264 the cortical meshwork. Cells were plated on tripod-shaped micropattern in order to observe  
265 cytoplasmic network dynamics above a large non-adhesive area. Although cells were not  
266 moving, the actin network displayed a dramatic and permanent reorganisation (Figure 6a,  
267 Video 6). This corroborated previous observations that cytoplasmic bundles can fuse with or  
268 split from the peripheral fibers<sup>9,43-46</sup> (Extended Data 6a). The mechanism supporting the  
269 remodeling of network architecture, and in particular the lateral translocation of bundles, is  
270 still unclear. Longitudinal contractile forces, along the bundle, can promote the lateral  
271 translocation of curved bundles<sup>9,46</sup>. Interestingly, rather straight bundles were also capable to



272 move laterally and fuse and split with adjacent bundles (Figure 6b). These movements happen  
273 in response to the production of lateral forces, normal to the bundle, without any translocation  
274 of their anchorages (see arrows in Figure 6b and Video 7), suggesting that lateral forces were  
275 produced by the contractile meshwork between bundles, as recently suggested by others<sup>47</sup>.

276 Interestingly, in regions of lower density of bundles, new bundles were found capable  
277 of emerging from the cortical meshwork (Figure 6c and corresponding Video 8, Extended  
278 Data 6a). Without any visible splitting event from adjacent bundles, the new bundle appeared  
279 as a thin line of higher density forming first near a former attachment to the substrate and  
280 elongating toward a pre-existing bundle ( $t=0$  to  $t=30$  min). Bundle thickening was  
281 homogeneous all along its length, suggesting further reinforcement by lateral recruitment of  
282 cortical filaments ( $t=30$  to  $t=45$  min). Interestingly, the newly formed bundle then expanded  
283 into a wider structure and eventually split into several bundles (indicated by orange arrows in  
284 Figure 6d and Video 8). This lateral expansion and splaying further supported the existence of  
285 lateral forces associated to the contractility of the adjacent cortical meshwork. The expansion  
286 and merging of bundles sometimes led to the assembly of quasi-continuous structure in which  
287 individual bundles were almost impossible to distinguish (Figure 6e)<sup>47</sup>. This showed that  
288 stress fibers were not only connected to the cortical meshwork but could also stem from the  
289 coalescence of filaments in the cortex; an assembly process that further accounts for their  
290 complete embedding in this meshwork (Figure 6f).

291 Bundles appeared more static above an adhesive area than above a non-adhesive area  
292 (Extended Data 6b,c). This further suggested that the capacity to glide in the cortex helped the  
293 coalescence of thin bundles into larger stress fibers, whereas the presence of anchorage to the  
294 underlying extra-cellular matrix kept thin bundles static and separated. This absence of  
295 coalescence of small bundles into larger fibers above adhesive regions could account for  
296 lower energy release induced by bundle ablation in pill-shaped as compared to dumbbell-  
297 shaped micropatterns (Extended Data 6d) and for the difference in total cellular force  
298 production in geometries with various level of no-adhesive area (Figure 1c,d and Extended  
299 Data 1d).

300

301

302

303 **Discussion**

304

305 Our investigation of the force production by different actin networks revealed  
306 unexpected properties of the intracellular actomyosin machinery that appeared essential to  
307 integrate and transmit forces at the level of the cell. We demonstrated that the stress fibers are  
308 fully embedded in a contractile cortical actin network, and are not independent structures or  
309 structures with only discrete connections to other stress fibers. This meshwork of stress fibers  
310 and cortical filaments form a mechanical continuum (Figure 6f). Our conclusion is in  
311 agreement with the previous ultrastructural observations of the cortical-actin-network  
312 connections to stress fibers and the more recent electron-microscopy demonstration that these  
313 connections depend on filamin A<sup>21,48,49</sup>. It also fits well with high-resolution imaging  
314 showing self-alignment of myosinII contractile ministacks in random meshworks<sup>50</sup> and  
315 lateral interactions of myofibrils, which support a long range self-organization of contractile  
316 structures<sup>47,51</sup>. Hence we found that contractile forces generated by the stress fiber are not  
317 only manifested at stress fiber anchorage points but are also propagated across the entire cell  
318 via the cortical meshwork. Also, we demonstrated that the contraction of the cortical  
319 meshwork actively contributes to traction force transmission to focal adhesions, thereby  
320 impacting the overall magnitude of contractile energy of the cell.

321 The mechanical interdependence of stress fibers and the cortical meshwork was  
322 supported by visualization of the network architecture in that filaments in the cortical  
323 meshwork tended to align with closer proximity to the stress fiber (Figure 6f). This suggested  
324 that the randomly orientated filaments in the cortical network were converted into bundles of  
325 aligned filaments the nearer they were to the stress fiber, perhaps in a self-amplifying  
326 mechanism in which the bundle reinforces the tension in the stress fiber. We suspect this  
327 interconversion mechanism between the thin and non-attached filaments of the cortical  
328 network and bundled filaments to be essential for the rapid modulation of the production of  
329 traction forces, in response to changes of geometrical and mechanical cues.

330

## 331 REFERENCES

- 332 1. Katoh, K., Kano, Y., Masuda, M. & Onishi, H. Isolation and Contraction of the Stress Fiber. *Mol. Biol. Cell* **9**, 1919–1938 (1998).
- 333 2. Chrzanowska-Wodnicka, M. & Burridge, K. Rho-stimulated contractility drives the formation of stress
- 334 fibers and focal adhesions. *J. Cell Biol.* **133**, 1403–15 (1996).
- 335 3. Naumanen, P., Lappalainen, P. & Hotulainen, P. Mechanisms of actin stress fibre assembly. in *Journal*
- 336 *of Microscopy* **231**, 446–454 (2008).
- 337 4. Chugh, P. *et al.* Actin cortex architecture regulates cell surface tension. *Nat. Cell Biol.* **19**, 689–697
- 338 (2017).
- 339 5. Chugh, P. & Paluch, E. K. The actin cortex at a glance. *J. Cell Sci.* **131**, jcs186254 (2018).
- 340 6. Livne, A. & Geiger, B. The inner workings of stress fibers - from contractile machinery to focal
- 341 adhesions and back. *J. Cell Sci.* **129**, 1293–1304 (2016).
- 342 7. Kurzawa, L. *et al.* Dissipation of contractile forces: the missing piece in cell mechanics. *Mol. Biol. Cell*
- 343 **28**, 1825–1832 (2017).
- 344 8. Burridge, K. & Guilluy, C. Focal adhesions, stress fibers and mechanical tension. *Exp. Cell Res.* **343**,
- 345 14–20 (2016).
- 346 9. Hotulainen, P. & Lappalainen, P. Stress fibers are generated by two distinct actin assembly mechanisms
- 347 in motile cells. *J. Cell Biol.* **173**, 383–94 (2006).
- 348 10. Schulze, N. *et al.* FHOD1 regulates stress fiber organization by controlling the dynamics of transverse
- 349 arcs and dorsal fibers. *J. Cell Sci.* **127**, 1379–1393 (2014).
- 350 11. Tojkander, S., Gateva, G. & Lappalainen, P. Actin stress fibers--assembly, dynamics and biological
- 351 roles. *J. Cell Sci.* **125**, 1855–64 (2012).
- 352 12. Tojkander, S., Gateva, G., Husain, A., Krishnan, R. & Lappalainen, P. Generation of contractile
- 353 actomyosin bundles depends on mechanosensitive actin filament assembly and disassembly. *Elife* **4**,
- 354 e06126 (2015).
- 355 13. Burnette, D. T. *et al.* A role for actin arcs in the leading-edge advance of migrating cells. *Nat. Cell Biol.*
- 356 **13**, 371–382 (2011).
- 357 14. Shemesh, T., Verkhovskiy, A. B., Svitkina, T. M., Bershadsky, A. D. & Kozlov, M. M. Role of focal
- 358 adhesions and mechanical stresses in the formation and progression of the lamellipodium-lamellum
- 359 interface [corrected]. *Biophys. J.* **97**, 1254–64 (2009).
- 360 15. Wang, N., Butler, J. P. & Ingber, D. E. Mechanotransduction across the cell surface and through the
- 361 cytoskeleton. *Science (80-. )*. **260**, 1124–1127 (1993).
- 362 16. Hu, S. *et al.* Intracellular stress tomography reveals stress focusing and structural anisotropy in
- 363 cytoskeleton of living cells. *Am. J. Physiol. Cell Physiol.* **285**, C1082–C1090 (2003).
- 364 17. Cai, Y. *et al.* Cytoskeletal coherence requires myosin-IIA contractility. *J. Cell Sci.* **123**, 413–23 (2010).
- 365 18. Tanner, K., Boudreau, A., Bissell, M. J. & Kumar, S. Dissecting regional variations in stress fiber
- 366 mechanics in living cells with laser nanosurgery. *Biophys. J.* **99**, 2775–2783 (2010).
- 367 19. Kumar, S. *et al.* Viscoelastic retraction of single living stress fibers and its impact on cell shape,
- 368 cytoskeletal organization, and extracellular matrix mechanics. *Biophys. J.* **90**, 3762–73 (2006).
- 369 20. Chang, C.-W. & Kumar, S. Vinculin tension distributions of individual stress fibers within cell-matrix
- 370 adhesions. *J. Cell Sci.* **126**, 3021–3030 (2013).
- 371 21. Kumar, A. *et al.* Filamin A mediates isotropic distribution of applied force across the actin network. *J.*
- 372 *Cell Biol.* **218**, 2481–2491 (2019).
- 373 22. Kassianidou, E., Brand, C. A., Schwarz, U. S. & Kumar, S. Geometry and network connectivity govern
- 374 the mechanics of stress fibers. *Proc. Natl. Acad. Sci.* **114**, 2622–2627 (2017).
- 375 23. Smith, M. A. *et al.* A Zyxin-Mediated Mechanism for Actin Stress Fiber Maintenance and Repair. *Dev.*
- 376 *Cell* **19**, 365–376 (2010).
- 377 24. Chapin, L. M., Blankman, E., Smith, M. A., Shiu, Y. & Beckerle, M. C. Lateral Communication
- 378 between Stress Fiber Sarcomeres Facilitates a Local Remodeling Response. *Biophysj* **103**, 2082–2092
- 379 (2012).
- 380 25. Rossier, O. M. *et al.* Force generated by actomyosin contraction builds bridges between adhesive
- 381 contacts. *EMBO J.* **29**, 1055–68 (2010).
- 382 26. Stachowiak, M. R. & O’Shaughnessy, B. Recoil after Severing Reveals Stress Fiber Contraction
- 383 Mechanisms. *Biophys. J.* **97**, 462–471 (2009).
- 384 27. Luo, Y., Xu, X., Lele, T. P., Kumar, S. & Ingber, D. E. A multi-modular tensegrity model of an actin
- 385 stress fiber. *J. Biomech.* **41**, 2379–2387 (2008).
- 386 28. Besser, A., Colombelli, J., Stelzer, E. H. K. & Schwarz, U. S. Viscoelastic response of contractile
- 387 filament bundles. *Phys. Rev. E - Stat. Nonlinear, Soft Matter Phys.* **83**, 1–12 (2011).
- 388 29. Kassianidou, E. & Kumar, S. A biomechanical perspective on stress fiber structure and function.
- 389

390 *Biochim. Biophys. Acta - Mol. Cell Res.* **1853**, 3065–3074 (2015).

391 30. Guthardt Torres, P., Bischofs, I. & Schwarz, U. S. Contractile network models for adherent cells. *Phys.*  
392 *Rev. E* **85**, 1–13 (2012).

393 31. Bischofs, I. B., Klein, F., Lehnert, D., Bastmeyer, M. & Schwarz, U. S. Filamentous network mechanics  
394 and active contractility determine cell and tissue shape. *Biophys. J.* **95**, 3488–96 (2008).

395 32. Oakes, P. W., Banerjee, S., Marchetti, M. C. & Gardel, M. L. Geometry Regulates Traction Stresses in  
396 Adherent Cells. *Biophys. J.* **107**, 825–833 (2014).

397 33. Linsmeier, I. *et al.* Disordered actomyosin networks are sufficient to produce cooperative and telescopic  
398 contractility. *Nat. Commun.* **7**, 12615 (2016).

399 34. Von Erlach, T. C. *et al.* Cell-geometry-dependent changes in plasma membrane order direct stem cell  
400 signalling and fate. *Nat. Mater.* **17**, 237–242 (2018).

401 35. Théry, M., Pépin, A., Dressaire, E., Chen, Y. & Bornens, M. Cell distribution of stress fibres in response  
402 to the geometry of the adhesive environment. *Cell Motil. Cytoskeleton* **63**, 341–55 (2006).

403 36. Mandal, K., Wang, I., Vitiello, E., Orellana, L. A. C. & Balland, M. Cell dipole behaviour revealed by  
404 ECM sub-cellular geometry. *Nat. Commun.* **5**, 5749 (2014).

405 37. Peterson, L. J. *et al.* Simultaneous stretching and contraction of stress fibers in vivo. *Mol. Biol. Cell* **15**,  
406 3497–508 (2004).

407 38. Colombelli, J. *et al.* Mechanosensing in actin stress fibers revealed by a close correlation between force  
408 and protein localization. *J. Cell Sci.* **122**, 1665–1679 (2009).

409 39. Strahs, K. R. & Berns, M. W. Laser microirradiation of stress fibers and intermediate filaments in non-  
410 muscle cells from cultured rat heart. *Exp. Cell Res.* **119**, 31–45 (1979).

411 40. Koonce, M. P., Strahs, K. R. & Berns, M. W. Repair of laser-severed stress fibers in myocardial non-  
412 muscle cells. *Exp. Cell Res.* **141**, 375–384 (1982).

413 41. Kassianidou, E. *et al.* Extracellular Matrix Geometry and Initial Adhesive Position Determine Stress  
414 Fiber Network Organization during Cell Spreading. *Cell Rep.* **27**, 1897-1909.e4 (2019).

415 42. Toro-Nahuelpan, M. *et al.* Tailoring cryo-electron microscopy grids by photo-micropatterning for in-cell  
416 structural studies. *Nat. Methods* **17**, 50–54 (2020).

417 43. Hirata, H., Tatsumi, H. & Sokabe, M. Dynamics of actin filaments during tension-dependent formation  
418 of actin bundles. **1770**, 1115–1127 (2007).

419 44. Luo, W. *et al.* Analysis of the local organization and dynamics of cellular actin networks. *J. Cell Biol.*  
420 **202**, 1057–73 (2013).

421 45. Muller, A., Muller, S., Nasufovic, V., Arndt, H.-D. & Pompe, T. Actin stress fiber dynamics in laterally  
422 confined cells. *Integr. Biol. (Camb)*. **11**, 175–185 (2019).

423 46. Chen, T. *et al.* Large-scale curvature sensing by directional actin flow drives cellular migration mode  
424 switching. *Nat. Phys.* **15**, 393–402 (2019).

425 47. Hu, S. *et al.* Long-range self-organization of cytoskeletal myosin II filament stacks. *Nat. Cell Biol.* **19**,  
426 133–141 (2017).

427 48. Marek, L. F., Kelley, R. O. & Perdue, B. D. Organization of the cytoskeleton in square fibroblasts. *Cell*  
428 *Motil.* **2**, 115–130 (1982).

429 49. Svitkina, T. M. Ultrastructure of the actin cytoskeleton. *Curr. Opin. Cell Biol.* **54**, 1–8 (2018).

430 50. Fenix, A. M. *et al.* Expansion and concatenation of nonmuscle myosin IIA filaments drive cellular  
431 contractile system formation during interphase and mitosis. *Mol. Biol. Cell* **27**, 1465–1478 (2016).

432 51. Dasbiswas, K., Hu, S., Schnorrer, F., Safran, S. A. & Bershadsky, A. D. Ordering of myosin II filaments  
433 driven by mechanical forces: experiments and theory. *Philos. Trans. R. Soc. B Biol. Sci.* **373**, 20170114  
434 (2018).

435

436

## 437 METHODS

438 **Preparation of micropatterned polyacrylamide gels.** The preparation of patterned  
439 polyacrylamide hydrogels was performed according to the Mask method previously described  
440 in <sup>52</sup>. A quartz photomask was first cleaned through oxygenplasma (AST product, 300 W) for  
441 3.5 min at 200 W. Areas containing the patterns were then incubated with 0.1 mg/ml PLL-g-  
442 PEG (JenKem Technology ZL187P072) in 10mM HEPES pH 7.4, for 30 min. After de-  
443 wetting, the mask was exposed under deep-UV for 5 min. Next, patterns on the mask were  
444 incubated with a mix of 10 µg/ml fibronectin (#F1141, Sigma) and 20 µg/ml fibrinogen-  
445 Alexa-Fluor-647 conjugate (#F35200, Invitrogen) in 100mM sodium bicarbonate buffer  
446 pH=8.4 for 30 min. A mix of acrylamide (8%) and bis-acrylamide solution (0.264%) (Sigma)  
447 corresponding to the experimental Young modulus of 34.8 kPa was degassed for  
448 approximately 30 min, mixed with 0.2 µm PLL-PEG coated fluorescent beads (Fluorosphere  
449 #F8810, Life Technologies) and sonicated before addition of APS and TEMED. 25 µl of that  
450 solution was added on the micropatterned photomask, covered with a silanized coverslip  
451 (Silane, #M6514, Sigma) and allowed to polymerize for 25 min before being gently detached  
452 in the presence of sodium bicarbonate buffer. Micropatterns were stored overnight in sodium  
453 bicarbonate buffer at 4°C before plating cells.

454 **AFM measurements of the Young's modulus of acrylamide gels.** Gel stiffness was  
455 measured through nano-indentation using an atomic force microscope (Bruker Nanoscope)  
456 mounted with silica-bead-tipped cantilevers ( $r(\text{bead}) = 2.5 \mu\text{m}$ , nominal spring constant 0.06  
457  $\text{N m}^{-1}$ , Novascan Technologies). The sensitivity of the photodiode to cantilever deflection  
458 was determined by measuring the slope of a force-distance curve when pressing the cantilever  
459 onto a glass coverslip. The force constant of the cantilever was determined using the thermal-  
460 noise method included in the Bruker Nanoscope software. For each acrylamide/bis-  
461 acrylamide ratio used in the traction-force microscopy measurements, 27 force curves in 3 by  
462 3 grids were acquired (2 µm spacing between points) at three different locations on the gels.  
463 Before and during indentation experiments, gels were kept in PBS. Stiffness values from  
464 force curves were obtained using the NanoScope Analysis software, correcting for baseline  
465 tilt using the linear fitting option with the Hertz model and a Poisson ratio of 0.48 on the  
466 indentation curve.

467 **Preparation of micropatterned glass slides.** To increase the resolution of actin images,  
468 RPE-1 cells were grown on glass micropatterns prepared as previously described in <sup>53</sup>. Glass  
469 coverslips were spin-coated for 30 sec at 3000 rpm with adhesion promoter Ti-Prime  
470 (MicroChemicals), then heated for 5 min at 120°C and spin-coated again for 30 sec at 1000  
471 rpm with 1% polystyrene in toluene (Sigma). Coverslips were then oxidized by plasma  
472 (FEMTO, Diener Electronics) (19 sec, 30 W) and incubated for 30 min with 0.1 mg/ml PLL-  
473 g-PEG (PLL20K-G35-PEG2K, JenKem) in 10 mM HEPES pH 7.4. Dried coverslips were  
474 next exposed to deep-UV (UVO cleaner, Jelight) through a photomask (Toppan) for 5 min.  
475 Coverslips were incubated for 30 min with 10 µg/ml fibronectin (Sigma) and 20 µg/ml  
476 fibrinogen-Alexa-Fluor-647 conjugate (Invitrogen) in PBS (phosphate buffered saline) after  
477 UV exposure.

478 **Cell culture.** Human telomerase-immortalized retinal-pigmented epithelial cells (RPE1;  
479 Clontech) either expressing LifeAct-GFP or parental (Vignaud et al., 2012) were grown in a  
480 humidified incubator at 37°C and 5% CO<sub>2</sub> in DMEM/F12 medium supplemented with 10%  
481 fetal bovine serum and 1% penicillin/streptomycin (GIBCO/Life technologies). Cells were  
482 plated at approximately 15000 cells/ml on patterned polyacrylamide gels and left to spread for  
483 3 to 4 hours before imaging. The Arp2/3 complex was inhibited with CK869 (Sigma Aldrich  
484 C9124, 50µM). To down-regulate the expression of alpha-actinin, RPE1 cells were  
485 transfected with two set of siRNAs (Qiagen) using lipofectamine RNAi Max transfection  
486 reagent (Life Technologies) at a final concentration of 10 nM following the manufacturer's  
487 protocol. Strand sequences were: siACTN4 :5'-GCAGCAUCGUGGACUACAATT-3' ;  
488 siACTN1 :5'-GCACCAUCAUGGACCAUUATT-3'. COS7 cells (ATCC CRL-1651) were  
489 cultured in DMEM (Gibco) supplemented with 2 mM GlutaMAX (Gibco), 50 U/ml penicillin,  
490 50 µg/ml streptomycin (Penstrep, Gibco) and 10% foetal bovine serum (FBS; Gibco)<sup>55</sup>. Rat  
491 hippocampal neurons were cultured on 18 mm coverslips at a density of 6,000/cm from  
492 embryonic day 18 pups<sup>56</sup> following established guidelines of the French Animal Care and  
493 Use Committee (French Law 2013-118 of 1st February 2013) and approval of the local ethics  
494 committee (agreement 2019041114431531-V2 #20242). In these neuronal cultures, a small  
495 number of astrocytes (glial cells) such as the one shown in Figure 5 are present and were  
496 labelled and imaged.

497 **Immunostaining and labeling.** Cells were pre-permeabilized in 0.5% Triton X-100 in  
498 cytoskeleton buffer for 17 sec for p-MLC and alpha-actinin staining and then rapidly fixed in  
499 4% paraformaldehyde in cytoskeleton buffer 10% sucrose pH 6.1 for 15 min at room  
500 temperature. Cells were then washed twice with cytoskeleton buffer and incubated in  
501 quenching agent 0.1 M ammonium chloride for 10 min. For all conditions, after fixation, the  
502 cells were washed then blocked with 1.5% bovine serum albumin (BSA) for 45 minutes. The  
503 cells were incubated with appropriate dilutions of primary antibodies in PBS containing 1.5%  
504 BSA and 0.1% Tween overnight at 4°C in a humid chamber. For the primary antibodies, anti-  
505 phospho-myosin light chain 2 (#3671, Cell Signaling Technology), anti  $\alpha$ -actinin (#05-384,  
506 Merck Millipore, clone AT6/172), and anti-paxillin (#610051, BD Biosciences, clone 349)  
507 were used. After several washing steps, the coverslips were then incubated with secondary  
508 antibodies (Alexa-Fluor antibodies, Invitrogen) diluted in PBS with 1.5% BSA and 0.1%  
509 Tween for 1 h at room temperature in a humid chamber. After washing, Phalloidin-FITC  
510 (#P5282, Sigma) was incubated for 20 min. After washing, coverslips were then mounted  
511 onto slides using Prolong Gold antifade reagent with DAPI (#P36935, Invitrogen).  
512 Fluorescent Tetraspeck microspheres of 0.5 µm diameter (#T7281, Life Technologies) were  
513 in some cases incubated with the coverslip to provide an internal fluorescence intensity  
514 reference. Whenever needed, SirActin (SC001, Spirochrome) was used at a concentration of  
515 500 nM for 3 h to stain actin in living cells.

516 **STORM imaging.** After fixation and immunolabeling<sup>55</sup>, cells were incubated with  
517 phalloidin-Alexa-Fluor-647 (0.5 µM, Thermo Fisher) overnight at 4°C. After two quick rinses  
518 in phosphate buffer, RPE1 cells were mounted in a closed chamber in STORM buffer (Smart  
519 kit, Abbelight) and imaged by STORM as described previously<sup>57</sup> using an N-STORM

520 microscope (Nikon Instruments) equipped with an Ixon DU-897 camera (Andor) and  
521 controled with Nikon Elements. Phalloidin (0.25 $\mu$ M) was added in the STORM medium to  
522 mitigate progressive unbinding from actin filaments during imaging<sup>55</sup>. After locating a cell  
523 using low-intensity illumination, epifluorescence images were acquired in both the green and  
524 far-red channels. For STORM imaging of actin, the sample was continuously illuminated at  
525 647nm (full power) and a series of 60000 to 100000 images (256x256 pixels, 15 ms exposure  
526 time). The N-STORM software (Nikon Instruments) was used for the localization of single  
527 fluorophore activations. After filtering, localizations with more than 800 photons, the list of  
528 localizations was exported as a text file and the ThunderSTORM plugin<sup>58</sup> of Fiji was used to  
529 generate reconstructions.

530 **Image acquisition and photoablation.** Images of the different immunostainings and high-  
531 resolution time-lapse of actin dynamics on PILL and DUMBBELL micropatterns were  
532 acquired on a confocal microscope Zeiss LSM800 using a 63X magnification objective (Zen  
533 Blue version 2). Staining of p-MLC,  $\alpha$ -actinin and paxilin were imaged using an AiryScan  
534 detector. GaAsP detectors were used for DAPI and micropattern stainings. Traction-force  
535 mapping, together with regular RPE1-LA-GFP, actin-GFP (CellLight™ Actin-GFP, BacMam  
536 2.0 from ThermoFischer Scientific) or SirActin (SC001, Spirochrome) imaging, were  
537 performed on a confocal spinning-disk system (EclipseTi-E Nikon inverted microscope  
538 equipped with a CSUX1-A1 Yokogawa confocal head, an Evolve EMCCD camera from  
539 Roper Scientific, Princeton Instruments). Photoablation was performed on a spinning-disk  
540 system from Nikon using the iLas2 device (Gataca Systems) equipped with a passively Q-  
541 switched laser (STV-E, ReamPhotonics, France) at 355 nm producing 500 picoseconds  
542 pulses. Laser displacement, exposure time and repetition rate were controlled via ILas  
543 software interfaced with MetaMorph (Universal Imaging Corporation). Laser photoablation  
544 and subsequent imaging was performed with a 100X CFI S Fluor oil objective (MRH02900,  
545 Nikon) or a 60X CFI S PLAN FLUOR ELWD objective. The laser power delivered before  
546 the objective, measured in the same conditions as the one used to perform photoablation  
547 experiment, was around 0.5mW at 100% laser. According to the specifications of the  
548 objectives used, this corresponds approximately to 250  $\mu$ W delivered at the output of the  
549 objective. The stress-fiber punctual photoablation was performed on fly during live  
550 acquisition. For the stress-fiber shaving, photoablation was performed on a narrow region  
551 medial and parallel to the length of the fiber above the non-adhesive substrate on the  
552 hydrogel. In this case, 13 repetitions of 25 ms pulses were used with 100% of the 355nm laser  
553 power, corresponding to a pulse of approximately 450 ms. Cells showing leakage or local  
554 blebbing following ablation were excluded from the analysis.

555 **Measurement of cell traction forces with ImageJ.** Data were analysed with a set of macros  
556 in Fiji using the method previously described in<sup>59</sup>. Displacement fields were obtained from  
557 fluorescent bead images before and after removal of cells by trypsin treatment. Bead images  
558 were first paired and aligned to correct for experimental drift. Displacement field was  
559 calculated by particle imaging velocimetry (PIV) on the basis of normalized cross-correlation  
560 following an iterative scheme. Final vector-grid size ranged from 1.55  $\mu$ m X 1.55  $\mu$ m to 1.60  
561  $\mu$ m X 1.60  $\mu$ m depending on magnification. Erroneous vectors were discarded owing to their

562 low correlation value and replaced by the median value of the neighbouring vectors. Traction-  
563 force field was subsequently reconstructed by Fourier-transform traction cytometry, with a  
564 regularization parameter set to  $8 \times 10^{-11}$ . Force vectors located outside of the micropattern area  
565 were discarded. Force quadrant analysis: Cell-traction force was computed above. The  
566 traction-force field was divided into 4 zones using the two planes of symmetry of the  
567 dumbbell shape of the micropattern. In each zone, forces were summed-up vectorially. The  
568 resulting vector was then located at the center of the zone for display.

569 **Cryo-electron Tomography of micropatterned cells.** Gold mesh (Au) grids overlaid with a  
570 perforated (R1/4) SiO<sub>2</sub> film (Quantifoil Micro Tools, Jena, Germany) were micropatterned  
571 using a one-step passivation, and a DMD-based illumination combined with a photo-activator,  
572 as previously described<sup>42,60</sup> (Leonardo v4.12, Alveole Lab, France). RPE1 cells were seeded  
573 on fibronectin micropatterned grids at a density of  $8 \times 10^3$  cells/cm<sup>2</sup> for 20-35 min. Next,  
574 grids were transferred to a cell-free dish and incubated at 37°C with 5 % CO<sub>2</sub> to allow cell  
575 adhesion. Cells were vitrified 4-7 h post-transfer. Grids were blotted from the back side of the  
576 grid support film and immediately plunged into liquid ethane at liquid nitrogen temperature  
577 using a Leica EM GP plunger (Leica Microsystems, Vienna, Austria). Cell thinning and  
578 imaging is described in Supplementary Methods.

579 **Statistical analysis.** Statistical analysis and chart design was performed using Graphpad  
580 Prism 6 and R version 3.4.0 together with RStudio version 1.0.143.

581

## 582 **References**

- 583 52. Vignaud, T., Ennomani, H. & Théry, M. Polyacrylamide hydrogel micropatterning. *Methods Cell Biol.*  
584 **120**, 93–116 (2014).
- 585 53. Azioune, A., Carpi, N., Tseng, Q., Théry, M. & Piel, M. Protein micropatterns: A direct printing  
586 protocol using deep UVs. *Methods Cell Biol.* **97**, 133–46 (2010).
- 587 54. Vignaud, T. *et al.* Reprogramming cell shape with laser nano-patterning. *J. Cell Sci.* **125**, 2134–40  
588 (2012).
- 589 55. Jimenez, A., Friedl, K. & Leterrier, C. About samples, giving examples: Optimized Single Molecule  
590 Localization Microscopy. *Methods* **174**, 100–114 (2020).
- 591 56. Vassilopoulos, S., Gibaud, S., Jimenez, A., Caillol, G. & Leterrier, C. Ultrastructure of the axonal  
592 periodic scaffold reveals a braid-like organization of actin rings. *Nat. Commun.* **10**, 1–13 (2019).
- 593 57. Ganguly, a. *et al.* A dynamic formin-dependent deep F-actin network in axons. *J. Cell Biol.* **210**, 401–  
594 417 (2015).
- 595 58. Ovesný, M., Křížek, P., Borkovec, J., Švindrych, Z. & Hagen, G. M. ThunderSTORM: A comprehensive  
596 ImageJ plug-in for PALM and STORM data analysis and super-resolution imaging. *Bioinformatics* **30**,  
597 2389–2390 (2014).
- 598 59. Martiel, J.-L. *et al.* Measurement of cell traction forces with ImageJ. in *Methods in cell biology* **125**,  
599 269–287 (2015).
- 600 60. Toro-Nahuelpan, M. *et al.* Tailoring cryo-electron microscopy grids by photo-micropatterning for in-cell  
601 structural studies. *Protoc. Exch.* (2020). doi:10.21203/rs.2.12377/v1  
602

603

604



605 **Acknowledgements**

606 We thank the live microscopy facility MuLife of IRIG/DBSCI, funded by CEA Nanobio and  
607 labex Gral for equipment access and use. This work was supported by grants from European  
608 Research Council (741773, AAA) awarded to LB, (771599, ICEBERG) awarded to MT, from  
609 Agence Nationale de la recherche ANR (ANR-14-CE11-0003-01, MaxForce) awarded to LB  
610 and MT, and from US Army Research Office (grant W911NF-17-1-0417) to A.M.. J.M.  
611 acknowledges the EMBL for funding. M.T.-N. was supported by a fellowship from the  
612 EMBL Interdisciplinary (EI3POD) programme under Marie Skłodowska-Curie Actions  
613 COFUND (664726).

614 **Author contributions**

615 TV and LK performed most of the experiments. QT performed preliminary work related to  
616 fiber ablation and traction force microscopy. CC and AM conceived and run the model. CL  
617 performed STORM imaging. MTN and JM performed the cryo-ET. LB, AM, MT and LK  
618 designed the experiments, supervised the project and analyzed data.

619 **Competing interest**

620 The authors declare no competing or financial interests.

621 **Data Availability Statement.**

622 Raw data are available from the corresponding authors upon request.

623

624 **Code Availability Statement.**

625 Code is available from the corresponding authors upon request.

626 **FIGURE LEGENDS**

627

628 **Figure 1. The stress fiber sets the magnitude of the traction force exerted by the cell but**  
629 **remains under tension after photoablation**

- 630 a. Micropattern designs (60  $\mu\text{m}$  length) and their respective outcomes in actin-network  
631 architecture. Dumbbell shape (left): Actin stress fibers (thick black lines) form  
632 between the two adhesive disks (red). Pill shape (right): Formation of a continuous  
633 actin mesh.
- 634 b. Immunostainings of RPE1 cells spread on dumbbell-shaped (left panel) and pill-  
635 shaped polyacrylamide micropatterns (right panel), respectively. For each shape,  
636 single examples of representative cells are displayed. From top to bottom:  
637 micropatterns labeling (fibrinogen-Cy5); actin (phalloidin ATO-488); paxillin (Alexa-  
638 488); phosphorylated-Myosin light chain (CY3); alpha-actinin (CY3). Image scale bar  
639 = 10  $\mu\text{m}$ . N=3 independent experiments.
- 640 c. Traction-force maps of cells spread on dumbbell (left column) and pill micropatterns  
641 (right column) of 37  $\mu\text{m}$ , respectively. Upper images display traction-force maps of  
642 single representative cells (scale bar in Pa). Lower images show averaged traction-  
643 force maps of cells.
- 644 d. Scatter plot of the mechanical energies of single cells and associated p-value (two-  
645 tailed Mann-Whitney t-test,  $p < 0.0001$ , median is depicted) (Dumbbell shape  $n=160$   
646 cells,  $N=7$  experiments; pill shape  $n=107$ ,  $N=2$  experiments).
- 647 e. Force relaxation study upon peripheral stress-fiber photoablation. Left panel from top  
648 to bottom: Micropattern labeling (Fibrinogen-CY5); actin (LifeAct-GFP) before  
649 photoablation (0 sec) and after photoablation (10 sec, red arrow); corresponding  
650 traction-force maps of the initial forces; and traction-force maps after photoablation.  
651 Image scale bar = 10  $\mu\text{m}$ . Force scale bar in Pa.  $N=4$  experiments.
- 652 f. Scatter plot of individual released mechanical energies after stress-fiber photoablation  
653 (% of the initial mechanical energy) for  $n = 50$  cells,  $N = 4$  experiments. Mean is  
654 depicted.

655

656 **Figure 2. Stress fibers are connected to the surrounding actin cytoskeletal network**

- 657 a. From top to bottom: RPE1-actin-GFP time-lapse images. Stripes were photobleached  
658 at regular intervals along the stress fiber (at 10 sec, orange dashed lines);  
659 photoablation was then performed at the center of the stress fiber (at 25 sec, red  
660 arrow). Image scale bar = 10  $\mu\text{m}$ . N=2 experiments.
- 661 b. Corresponding kymograph with colored lines highlighting the retraction of the  
662 photobleached marks.
- 663 c. Normalized retraction distance was calculated by dividing the length of each retracted  
664 segment (between two marks) by its initial length. Corresponding retraction values  
665 were plotted as a function of the initial distance of the photobleached segment from  
666 the photoablation site for  $n = 264$  segments (44 cells analyzed from 2 experiments).  
667 Values were fitted with a linear regression (blue line depicts the line produced by  
668 linear regression minimizing squared error). 95% confidence intervals (-0.0243,-  
669 0.0132 indicated by the grey area) based on standard errors indicates a negative slope  
670 which is distinct from zero (isolated elastic fiber,  $p < 0.00001$ , two-tailed t-test). 22  
671 negative values were excluded from the analysis as corresponding to cells in which the  
672 photoablation was not efficient.
- 673 d. Illustration of two sequential photoablations (cuts) on the same stress fiber at distinct  
674 locations (Cut 1=red arrow; Cut 2=blue arrow). Time-lapse images of RPE1-LifeAct-  
675 GFP cells after the two sequential photoablations. Scatter plots of the released  
676 mechanical energy (percentage of the mechanical energy before photoablation, mean  
677 is depicted) for the two types of photoablation sequence ( $n=35$  cells, N=3  
678 experiments). The p-value from a two-tailed paired t-test is indicated on the plot  
679 ( $p < 0.0001$ ). Image scale bar = 10  $\mu\text{m}$ .
- 680 e. Illustration of two sequential photoablations (cuts) on the two stress fibers in the cell  
681 (Cut 1=red arrow; Cut 2=blue arrow). Time-lapse images of RPE1-LifeAct-GFP cells  
682 after 2 photoablations. Scatter plots of the released mechanical energy for the two  
683 types of photoablation protocols ( $n=11$  cells, N=1 experiment, mean is depicted). The  
684 p-value from a two-tailed paired t-test is indicated on the plot ( $p=0.836$ ). Image scale  
685 bar = 10  $\mu\text{m}$ .
- 686 f. Illustration of stress-fiber “shaving”, i.e. photoablation of a narrow region medial and  
687 parallel to the length of the fiber above the non-adhesive substrate on the hydrogel.  
688 The shaved region (dark area) sitting next to the stress fiber was highlighted in the  
689 yellow inset and corresponding zoomed images. Image scale bar = 10  $\mu\text{m}$ .
- 690 g. Illustration of shaving (purple dashed line) followed by two sequential photoablations  
691 (cuts) on the adjacent peripheral stress fiber (Cut 1=red arrow; Cut 2=blue arrow).  
692 RPE1 cells labeled with SiR-actin and their corresponding micropatterns (fibrinogen-  
693 CY5) in a time-sequence corresponding to the shaving (T=5 sec), the first  
694 photoablation (T=15 sec, red arrow) and the second photoablation (T=30 sec, blue  
695 arrow). Image scale bar = 10  $\mu\text{m}$ . N=3 experiments.
- 696 h. Scatter plot of the mechanical energy released by the second photoablation of the  
697 stress fiber (percentage of the initial mechanical energy), alone (Cut 2;  $n=35$  cells,  
698 N=3) or preceded by a shaving (Cut 2 after shav;  $n=20$  cells, N=4). Means are

699 depicted. The p-value of Mann-Whitney two-tailed t-test is indicated on the plot  
700 ( $p=0.0067$ ). 8 negative values were excluded from the analysis as corresponding to  
701 cells in which the photoablation was not efficient.

702

703 **Figure 3. Model with active contractile stress fibers embedded in an elastic central mesh**

- 704 a. Diagram illustrating all components in the model, including the isotropic elastic  
705 cortical mesh, contractile elastic fibers along the long edges of the mesh, and adhesive  
706 sites located along the short edges of the mesh.
- 707 b. Plot displaying simulated traction-force loss as a result of the stress fiber ablation and  
708 corresponding experimental data.  $n=50$  cells, mean is depicted.
- 709 c. Simulated kymograph of a stress fiber indicating the movement of the regularly-  
710 spaced markers after simulated photoablation. Plot of the associated retraction  
711 percentage of these markers as a function of the distance from the ablation site.
- 712 d. Predicted and experimental mechanical energy release after two sequential  
713 photoablations on the same stress fiber.  $n=35$  cells;  $N=3$  experiments, mean is  
714 depicted. The p-value from a two-tailed paired t-test is indicated on the plot  
715 ( $p<0.0001$ ).
- 716 e. Representative image of the dumbbell-shaped micropattern (fibrinogen-CY5) and  
717 RPE1-LifeAct-GFP cells displaying photoablation at a lateral side of the stress fiber  
718 (red arrow) and the associated relaxation traction force field after the photoablation.  
719 Image scale bar =  $10\ \mu\text{m}$ . Force scale bar in Pa.  $N=3$  experiments.
- 720 f. Spatial distribution of force relaxation along the stress fiber after stress-fiber  
721 photoablation (red star). Left panel: The release of traction forces was considered in  
722 partitioned zones of the cell, where the orange zone included half the stress fiber and  
723 the off-centered photoablation site, and the blue zone included the other half of the  
724 stress fiber. Right panel: Plot displaying the prediction of the model and the  
725 experimental measurements ( $n=47$  cells,  $N=4$  experiments, mean is depicted) for the  
726 magnitude of released forces (as a percentage of the total force release) with respect  
727 to these zones. The p-value from the two-tailed paired t-test is indicated on the plot  
728 ( $p=0.0016$ ).
- 729 g. Spatial distribution of force relaxation across the cell after stress-fiber photoablation  
730 (red star). Left panel: The release of traction forces was considered in partitioned  
731 zones of the cell, where the green zone included the stress fiber with photoablation  
732 site, and the purple zone included the stress fiber without photoablation. Right panel:  
733 Plot displaying the prediction of the model and the experimental measurements ( $n=47$   
734 cells,  $N=4$  experiments, mean is depicted) for the magnitude of released forces (as a  
735 percentage of the total force release) with respect to these zones.

736

737 **Figure 4. The cortical meshwork is contractile**

- 738 a. Scatter plot of the released mechanical energy (percentage of the total mechanical  
739 energy before photoablation) after shaving the stress fiber (n=94 cells, N=14  
740 independent experiments), i.e. the photoablation of a narrow region medial and  
741 parallel to the length of the fiber above the non-adhesive substrate on the hydrogel, a  
742 single photoablation (cut; n=50 cells, N=4 independent experiments) of the stress  
743 fiber, or a photoablation of the stress fiber after its shaving (shaving+cut; n=65 cells;  
744 N=14 independent experiments). p-values from two-tailed unpaired t-tests are  
745 indicated on the plot (p=0.0074 for cut vs shaving; p<0.0001 for cut vs shaving+cut).  
746 19 outliers were automatically removed from the analysis (remove outliers function of  
747 Prism).
- 748 b. Images of RPE1-LifeAct-GFP cells on the left panel depicting a stress fiber subject to  
749 shaving, a single photoablation (cut), and shaving plus photoablation; with the  
750 corresponding traction-force maps of the cells shown in the right panel. The same cell  
751 was represented to illustrate the shaving and shaving plus photoablation (top and  
752 bottom panels, respectively). Image scale bar = 10  $\mu\text{m}$ . Force scale bar in Pa. N=3  
753 experiments. Image scale bar = 10  $\mu\text{m}$ .
- 754 c. Diagram illustrating all components in the fully contractile model, including an  
755 isotropic contractile cortical mesh.
- 756 d. Mechanical energy released after stress fiber photoablation (red arrow). Plot  
757 displaying the predictions of the elastic model, the contractile model and the  
758 experimental measurements (n=50 cells).
- 759 e. Mechanical energy release after shaving (purple line). Plot displaying the predictions  
760 of the elastic model, the contractile model and the experimental measurements (n=94  
761 cells; N=14). 9 outliers were automatically removed from the plot (remove outliers  
762 function in Prism).
- 763 f. Sequential photoablations (cuts) on the same stress fiber at distinct locations (Cut  
764 1=red arrow; Cut 2=blue arrow). Predictions of the elastic model, the contractile  
765 model and experimental data (n=35 cells, N=3 experiments). P-value calculated from  
766 a two-tailed paired t-test.
- 767 g. Sequential photoablations (cuts) on the two stress fibers in the cell (Cut 1=red arrow;  
768 Cut 2=blue arrow). Predictions of the elastic model, the contractile model and  
769 experimental data (n=11 cells, N=1 experiment). P-value calculated from a two-tailed  
770 paired t-test.
- 771 h. Spatial distribution of force loss along the stress fiber after off-center stress-fiber  
772 photoablation (red star). The loss of traction forces was considered in partitioned  
773 zones of the cell, where the orange zone included half the stress fiber and the off-  
774 centered photoablation site, and the blue zone included the other half of the stress  
775 fiber. Plot displaying the prediction of the elastic model, the contractile model, and the  
776 experimental data (n=47 cells). P-value calculated from a Wilcoxon paired t-test.
- 777 i. Spatial distribution of force loss after off-center stress-fiber photoablation (red star).  
778 The loss of traction forces was considered in partitioned zones of the cell, where the  
779 green zone included the stress fiber with photoablation site, and the purple zone

780 included the stress fiber without photoablation. Plot displaying the prediction of the  
781 elastic model, the contractile model, and the experimental data (n=47 cells).  
782

783 **Figure 5. The stress fiber is fully embedded in the adjacent actin cortex.**

- 784 a. (i) Cryo-Scanning Electron Microscopy of a vitrified RPE cell adhered and fully  
785 spread on a dumbbell-shape micropattern. Yellow rectangle indicates the putative  
786 location of the acquired tomograms. The yellow dashed line represents the dumbbell  
787 shape pattern size and position. Scale bar: 20  $\mu\text{m}$ . (ii) Tomographic slice (6.8 nm  
788 thickness) in a second cell. Scale bar: 200 nm. Yellow arrow points at the plasma  
789 membrane, the white arrows at actin filaments forming a bundle. (iii) Perspective view  
790 of the 3D rendering of the actin filament network from (ii). Blue-to-red color map of  
791 actin filaments represent the angular distribution (ranging from  $0^\circ$  to  $90^\circ$ ) relative to  
792 the z-plane of the tomogram. Plasma membrane depicted in gray. Blue arrows point at  
793 filaments connecting the bundle to adjacent networks and notably transverse filaments  
794 (color-coded in blue by their orientation). N=2 experiments.
- 795 b. Cellular cryo-ET of the stress fiber. Left: A tomographic slice, 6.8 nm thickness, (see  
796 Extended Data 5) showing the organization of actin filaments into a stress fiber and  
797 associated microtubules (MTs). Right: 3D rendering of the actin filament network and  
798 microtubules (purple). Yellow arrow points in the direction of the plasma membrane.  
799 Blue arrows point at the lateral part of the bundle that is oriented toward the cytoplasm  
800 and where filament density is lower than in the inner part of the bundle. Scale bar: 200  
801 nm. N=2 experiments.
- 802 c. STORM reconstructed image of the actin network (phalloidin-Alexa Fluor 647) in a  
803 RPE1 cell plated on a dumbbell-shaped micropattern on a glass substrate (scale bar=5  
804  $\mu\text{m}$ ). The interlacing of the peripheral stress fiber with the surrounding actin cortex  
805 was highlighted in the yellow inset and associated zoom-in below (scale bar=1  $\mu\text{m}$ ).  
806 N=1 experiment.
- 807 d. STORM reconstructed image of the actin network of a rat astrocyte and a COS-7 cell.  
808 The zoom on the astrocyte shows several bundle sizes in the cortex ranging from few  
809 aligned filaments to larger bundles of few hundreds of nanometers. The zoom on the  
810 COS cell shows the alignment and incorporation of individual filaments, or bundles of  
811 few filaments, at the end of a large bundle. Scale bar = 5  $\mu\text{m}$ . Zoom: Scale bar = 1  $\mu\text{m}$ .  
812 N=1 experiment.
- 813 e. Top: Immunostainings of phospho-Myosin Light Chain in a RPE1 cell spread on  
814 polyacrylamide dumbbell-shaped micropattern. Scale bar = 10  $\mu\text{m}$ . Zoom-in images of  
815 the yellow inset are displayed below for actin (phalloidin-ATO-488) and p-MLC. For  
816 the p-MLC, signal was displayed at saturation in order to highlight small myosin  
817 patches inside the actin mesh. Red arrows indicate the area where actin structures are  
818 organized into bundles and red rectangles demark areas devoid of actin-identifiable  
819 structures. Bottom: same with alpha-actinin. N=3 experiments.

820

821

822



823 **Figure 6. Emergence and translocation of cytoplasmic bundles in the cortical meshwork**

824

825

826 a. Live imaging of RPE1-LifeAct-GFP cells on tripod-shaped micropattern showing the  
827 global and permanent remodelling of network architecture, suggestive of a complex  
828 interplay of longitudinal and lateral forces on cytoplasmic bundles. See corresponding  
829 Video 5. N=1 experiment. Scale bar = 10  $\mu\text{m}$ .

830 b. Live imaging of RPE1-LifeAct-GFP cells on tripod-shaped micropattern highlighting  
831 network reconfiguration by lateral translocation of cytoplasmic bundles in the absence  
832 of anchorage displacement (red arrows). See corresponding Video 6. N=1 experiment.  
833 Scale bar = 10  $\mu\text{m}$ .

834 c. Live imaging of RPE1-LifeAct-GFP cells on tripod-shaped micropattern revealing the  
835 emergence of cytoplasmic bundles from the cortical meshwork (in between red  
836 arrows). See corresponding Video 7. N=1 experiment. Scale bar = 10  $\mu\text{m}$ .

837 d. Live imaging of RPE1-LifeAct-GFP cells on tripod-shaped micropattern showing the  
838 lateral expansion of a bundle (red arrow), its splaying into a wider structure (orange  
839 arrows) and its re-coalescence into several adjacent bundles (magenta arrows). See  
840 corresponding Video 7. N=1 experiment. Scale bar = 10  $\mu\text{m}$ .

841 e. RPE1-LifeAct-GFP cells on tripod-shaped micropattern displaying a dense and quasi-  
842 continuous network of cytoplasmic bundles. N=1 experiment.

843 In all panels, time is indicated in hours and minutes. Scale bar = 10  $\mu\text{m}$ .

844 f. Schematic representation of the stress fiber anchored at its two edges on the substrate  
845 via focal adhesions (blue disks) as a fully embedded structure within the surrounding  
846 contractile actin cortex (myosins are represented by blue bow-ties).

847

848

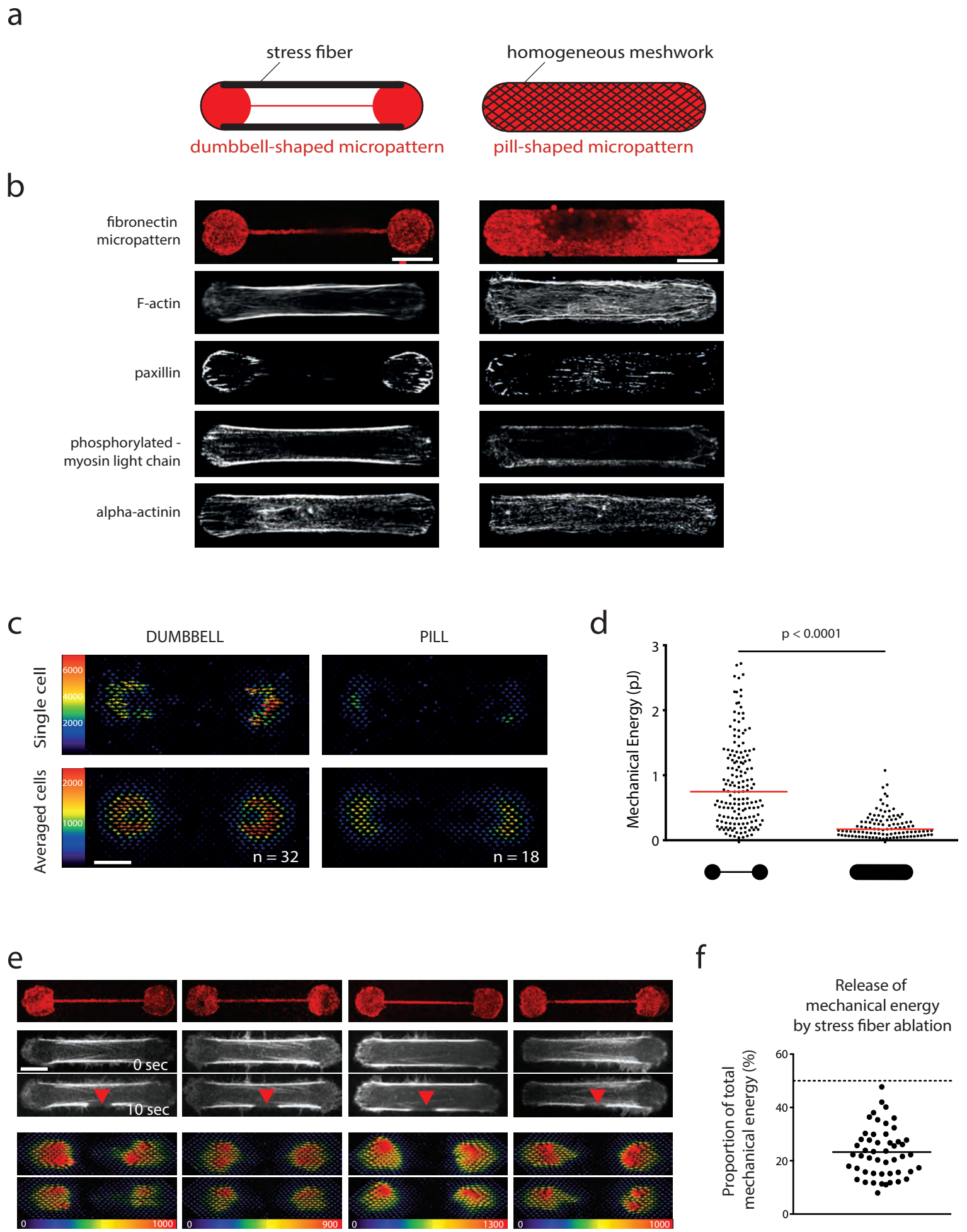


Figure 1

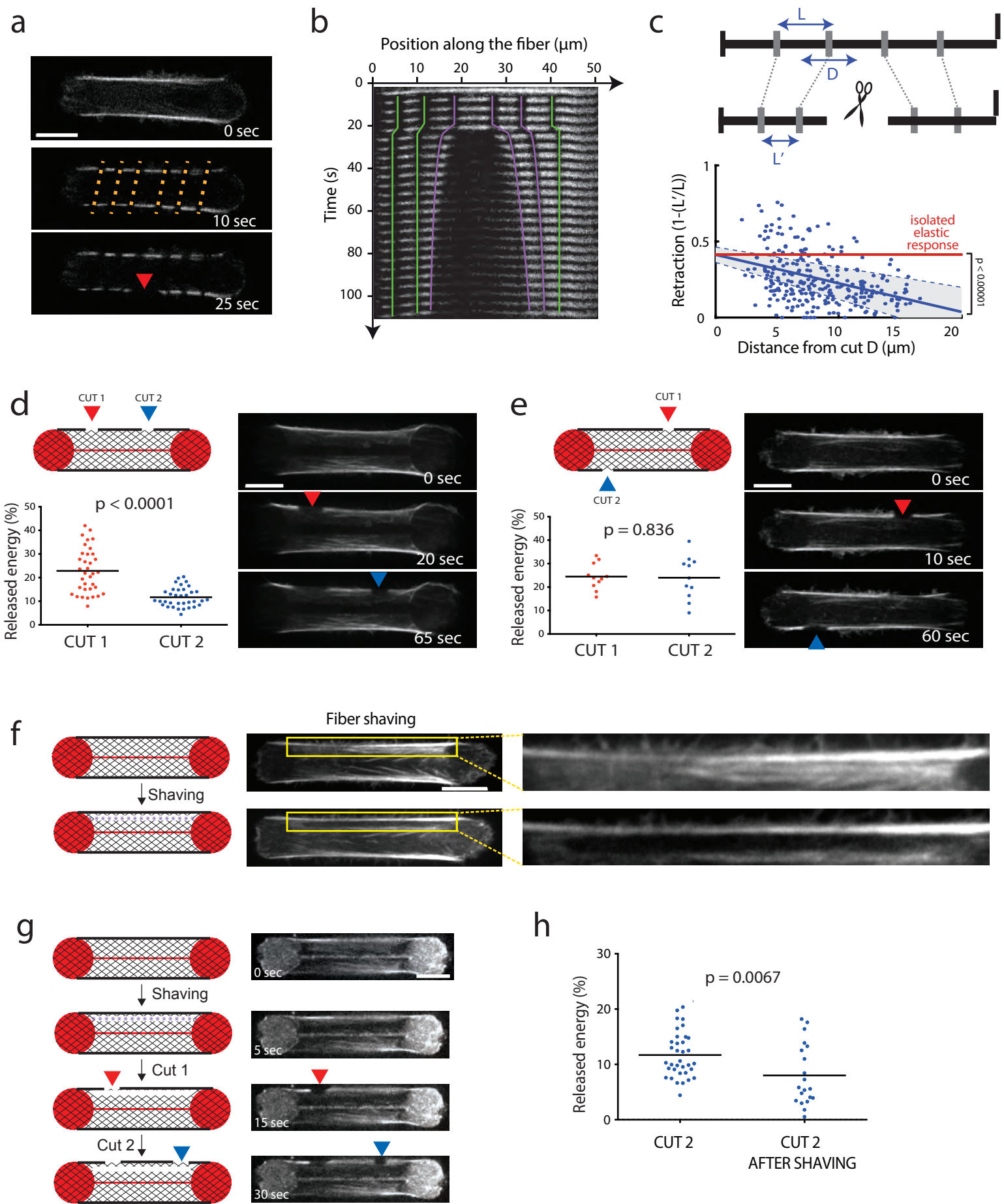


Figure 2

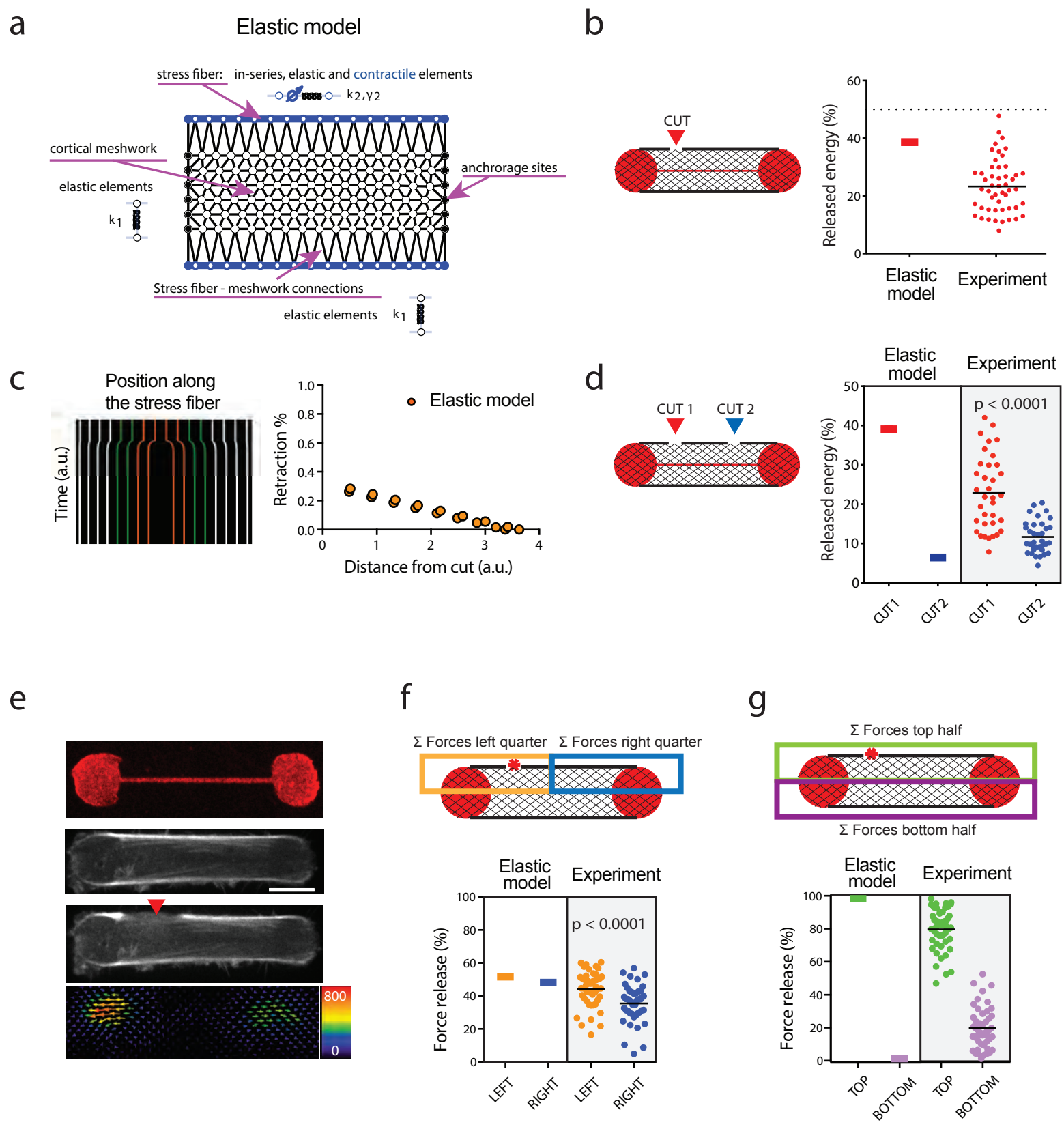


Figure 3

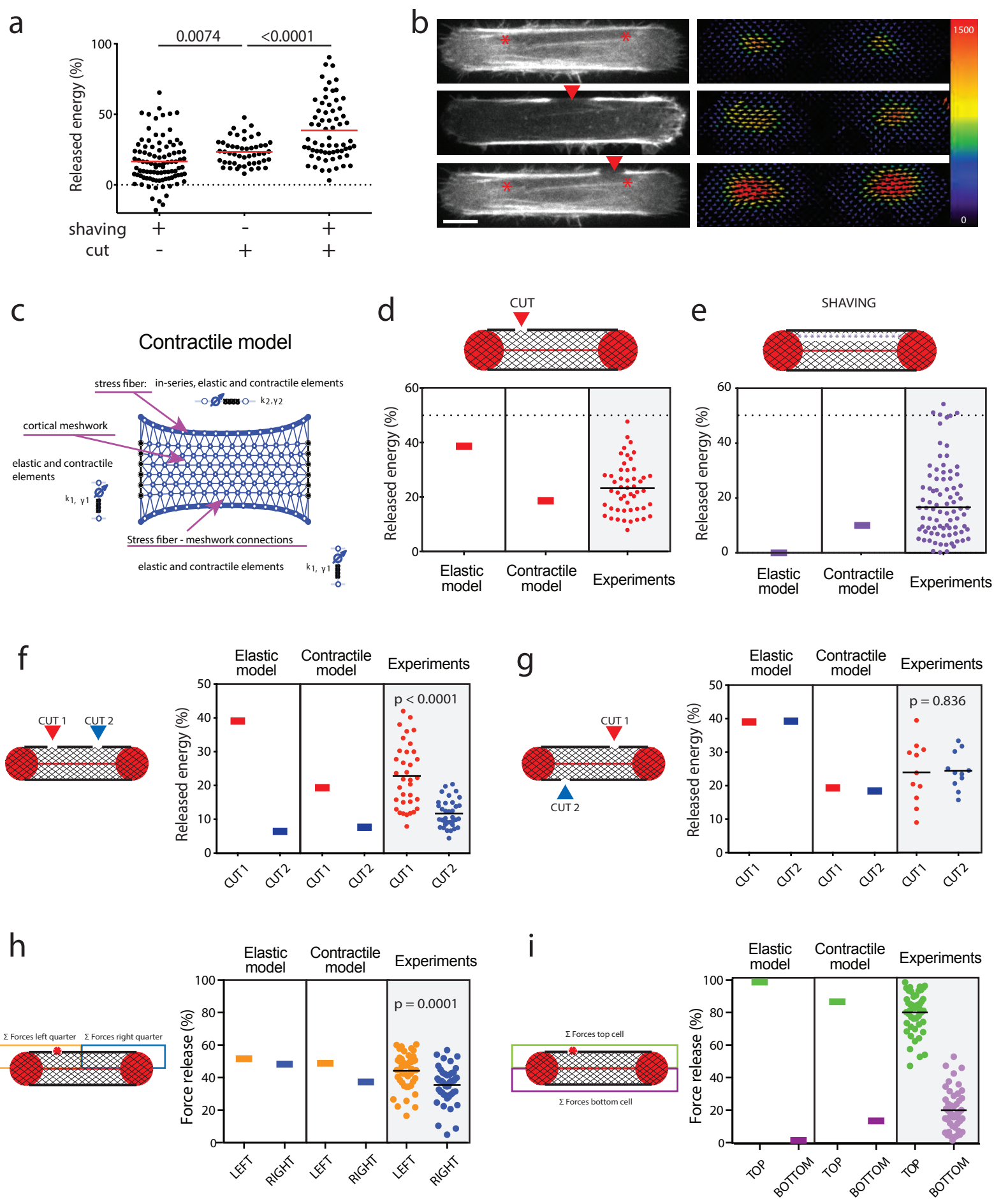


Figure 4

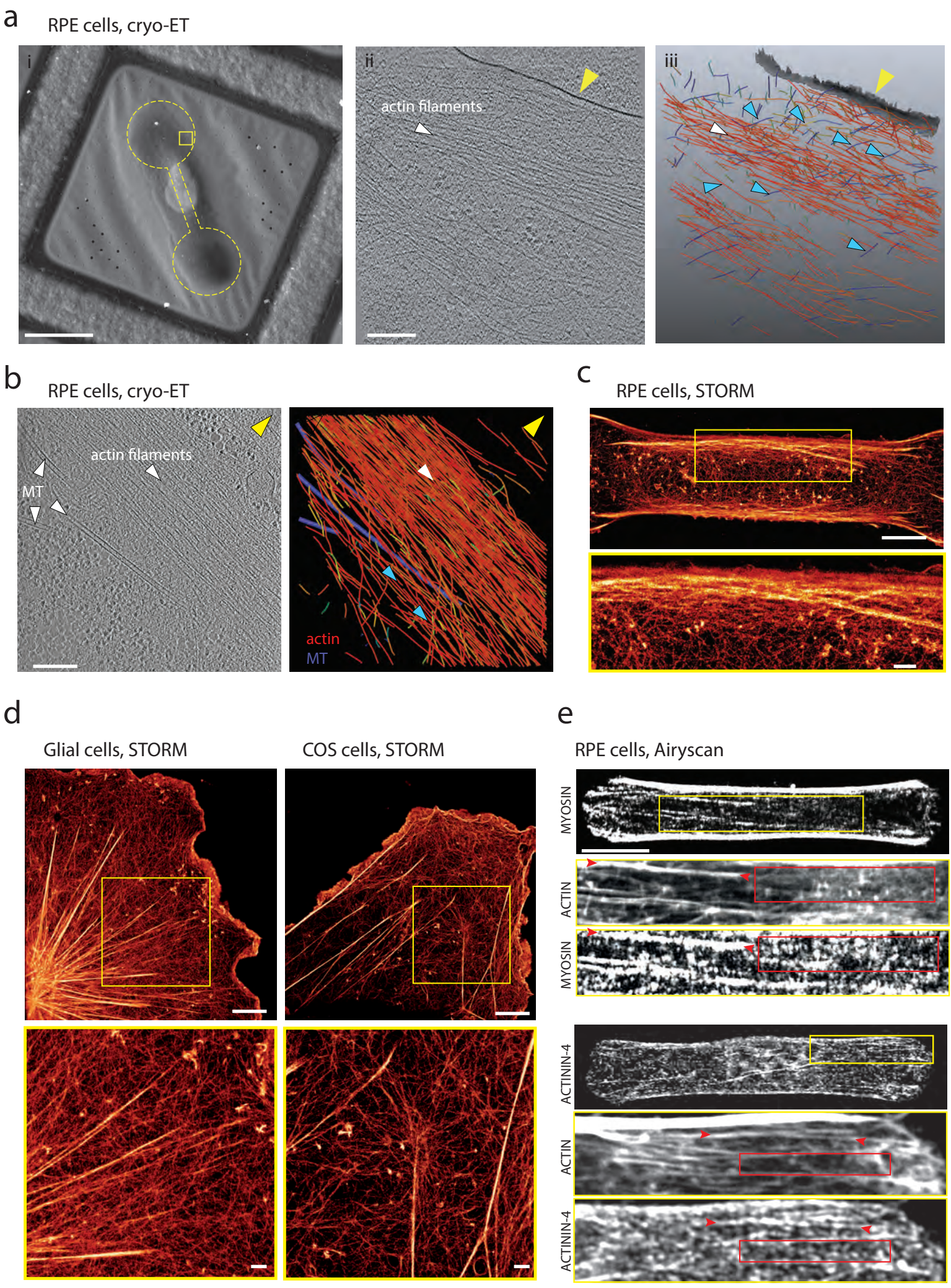


Figure 5

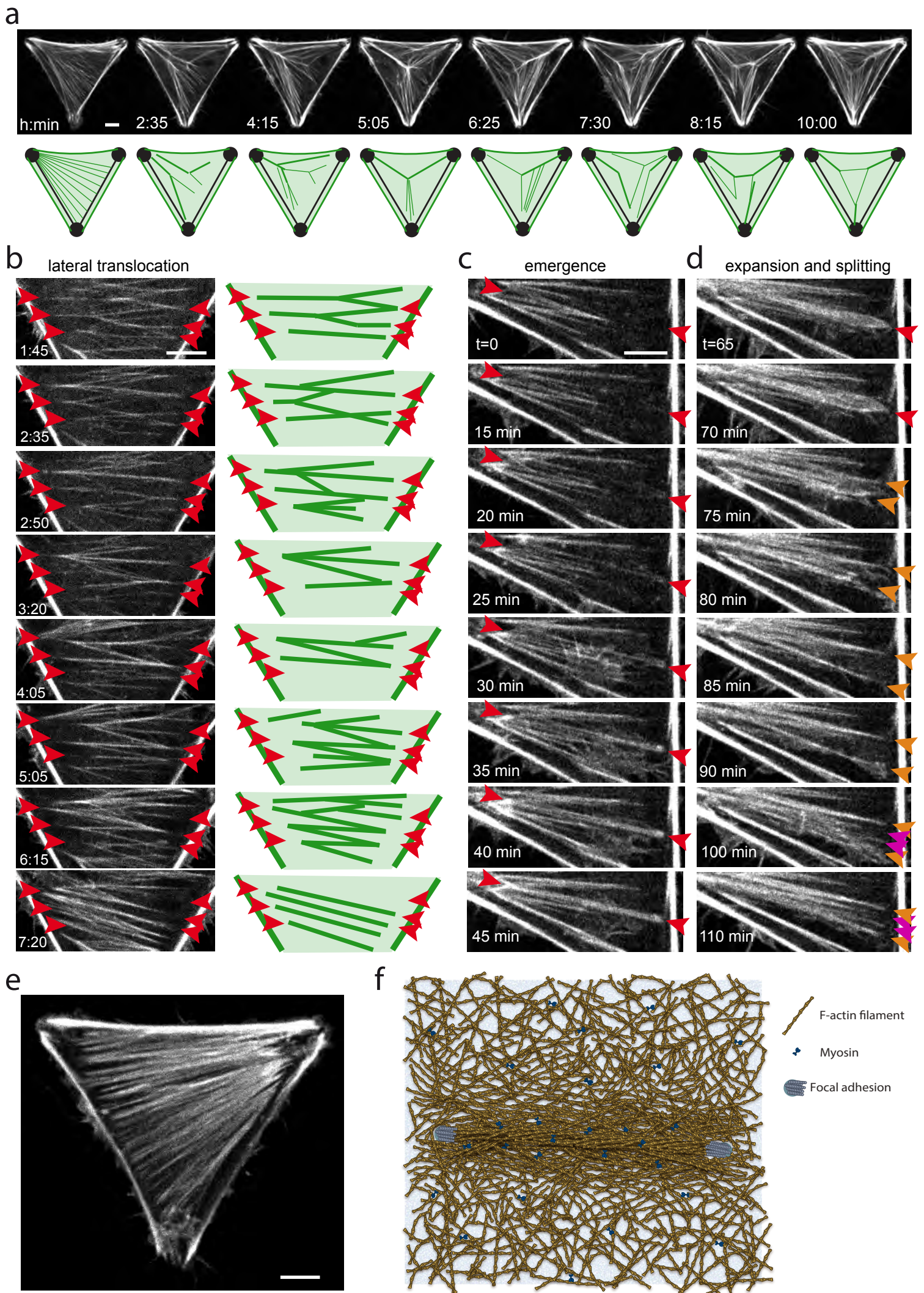
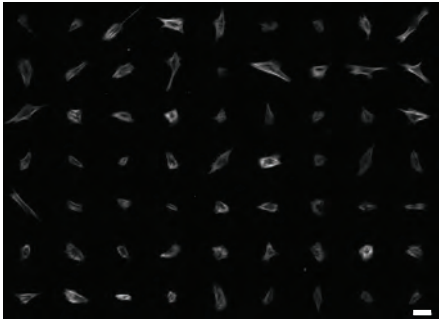
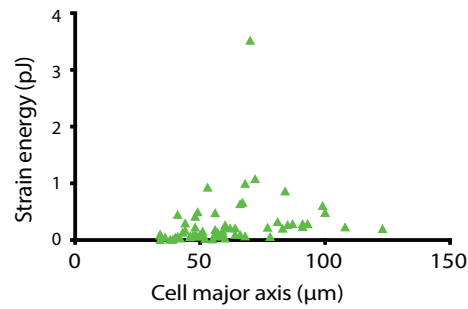


Figure 6

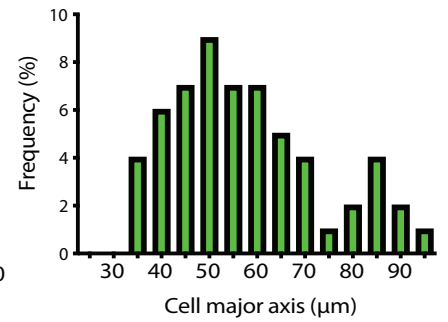
a



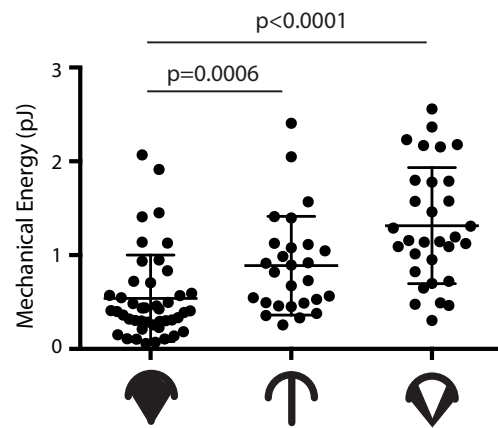
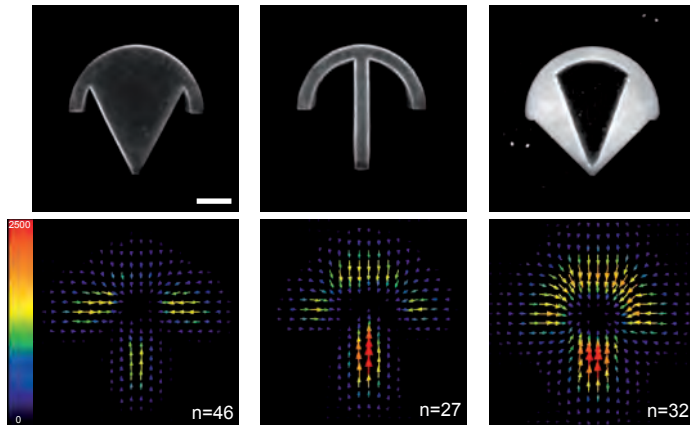
b



c

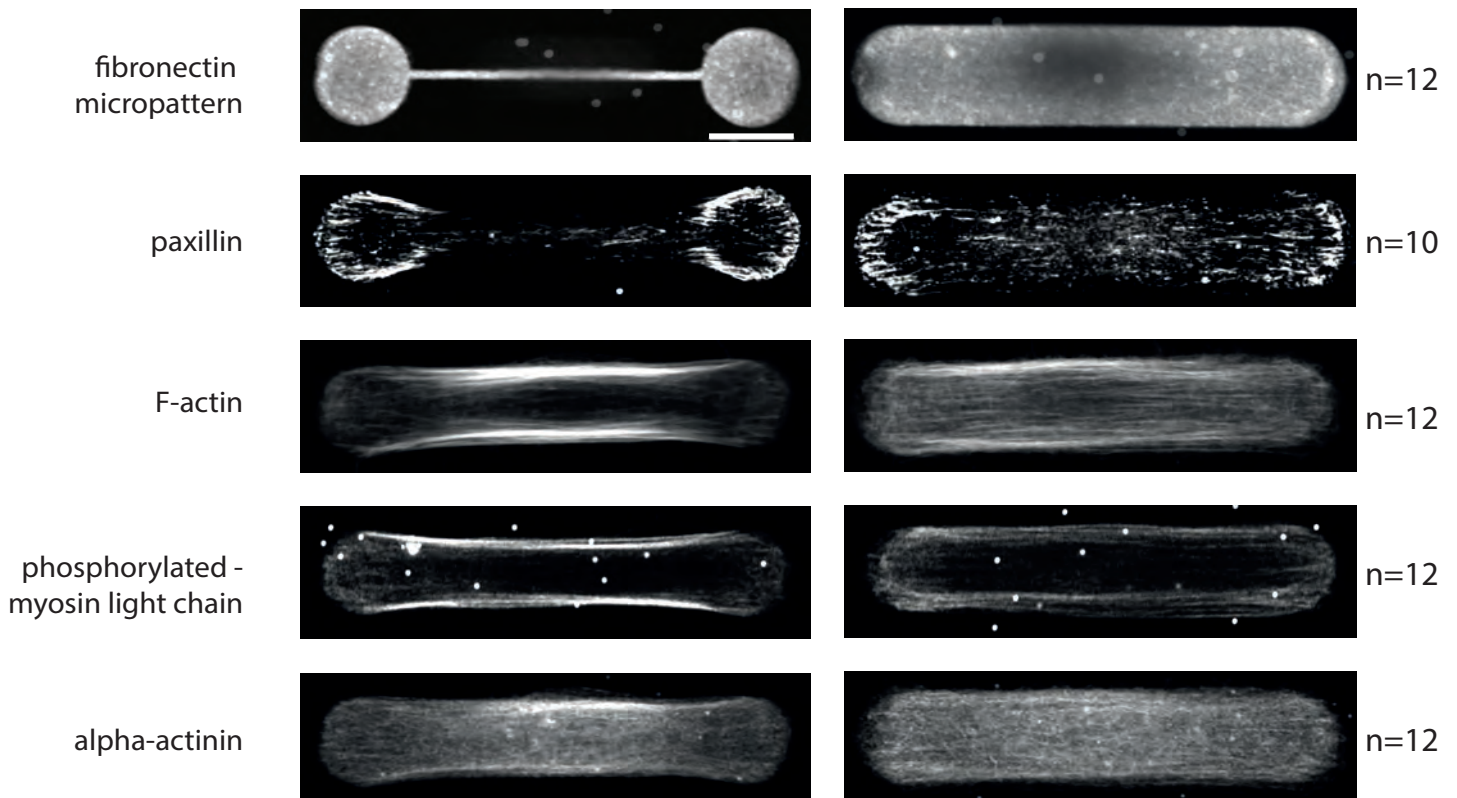


d



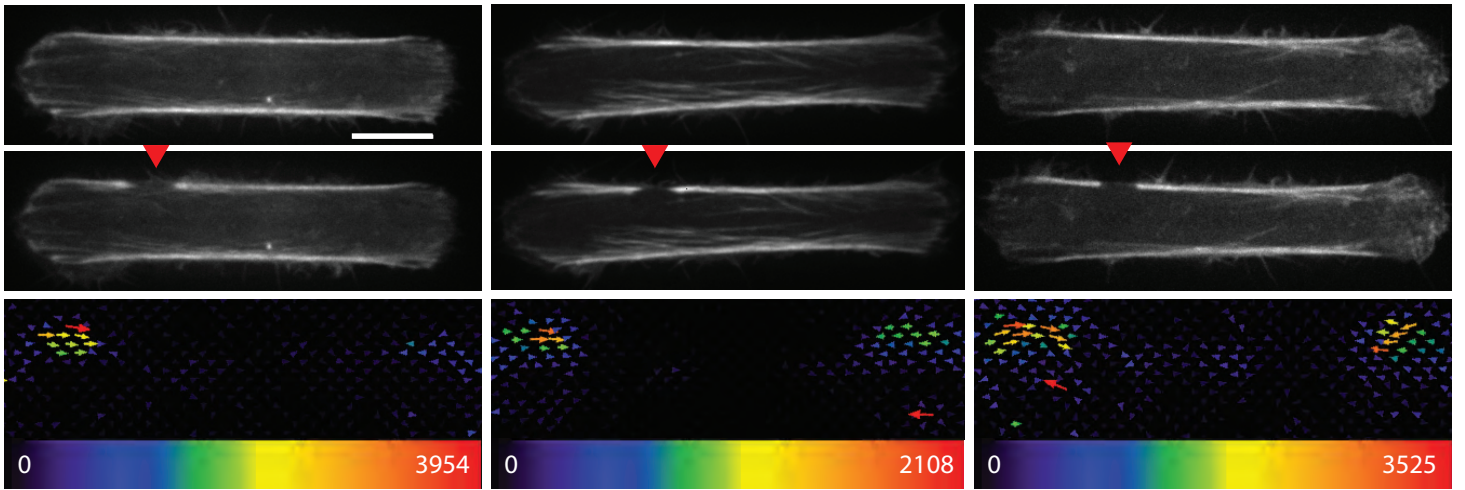
e

Averaged labellings

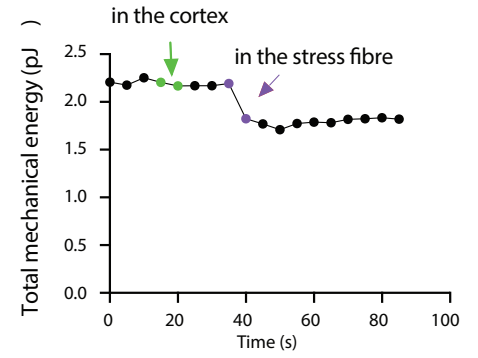
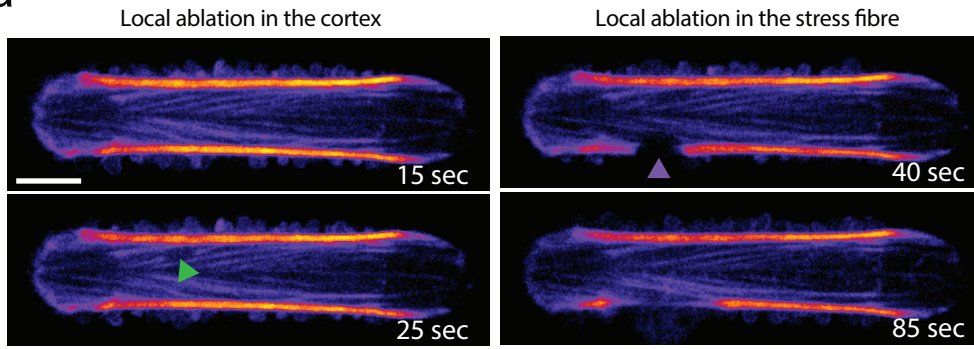
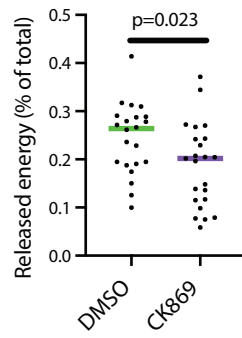
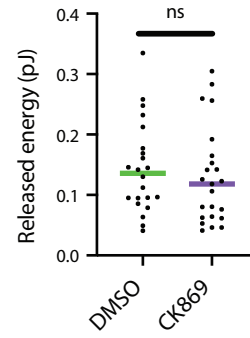
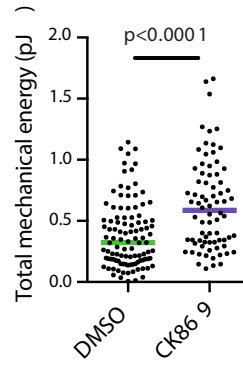
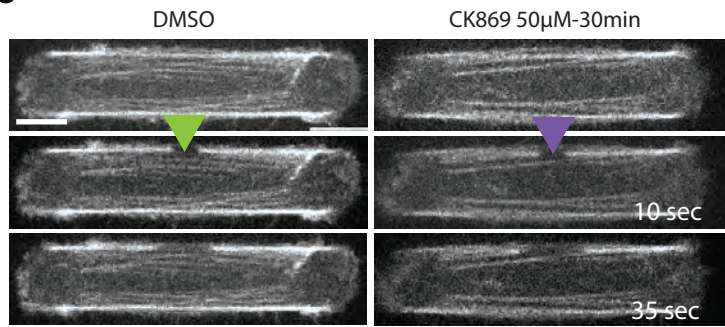


Extended Data 1

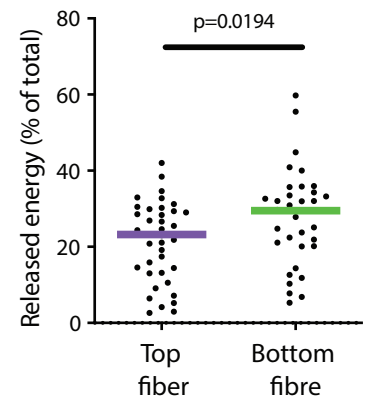
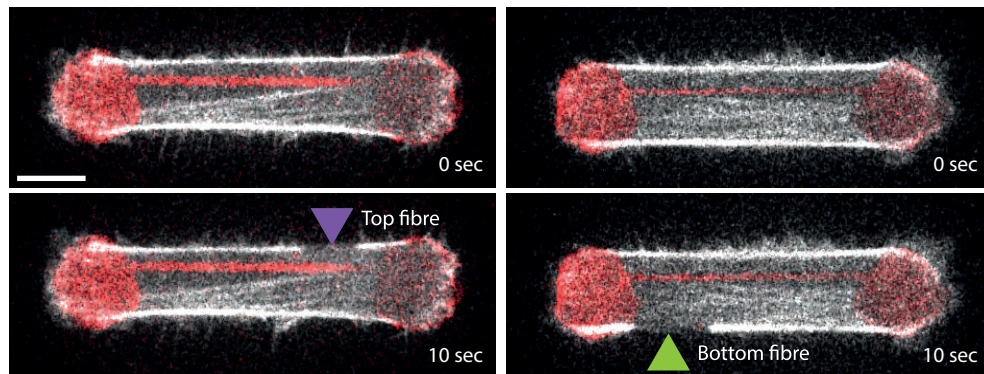
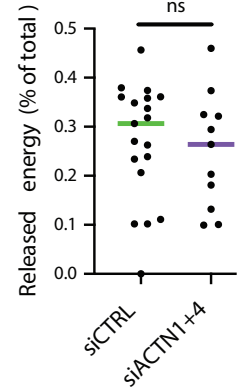
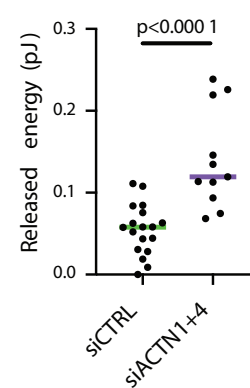
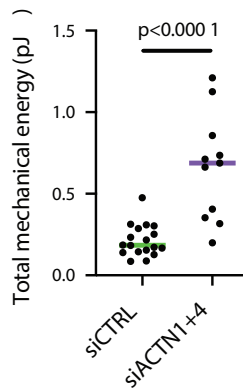
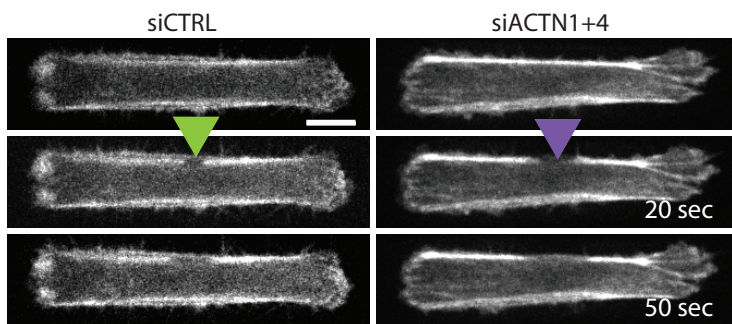




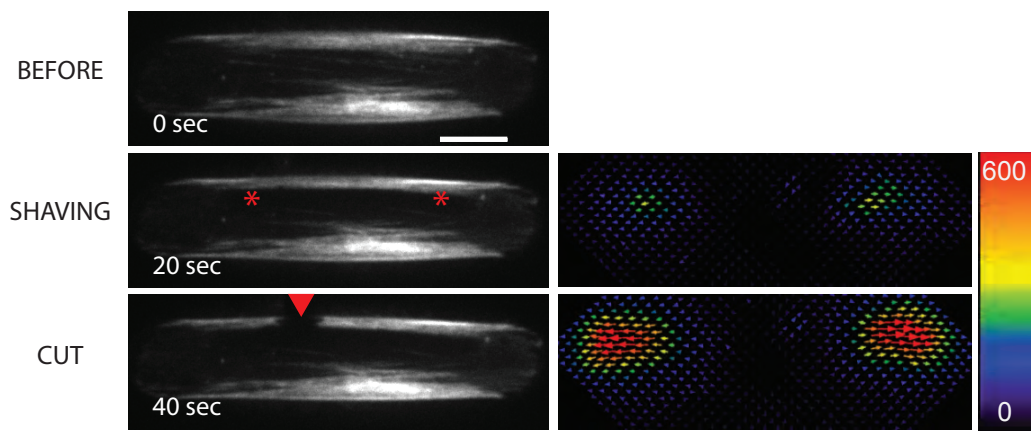
Extended Data 2

**a****b****c**

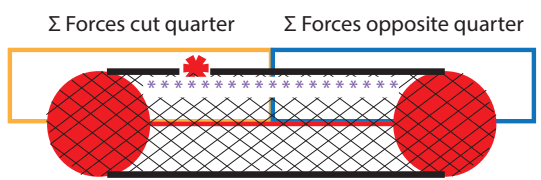
Asymmetric micropattern

**d**

a



b



c

